

PREPARED FOR SUBMISSION TO JCAP

Gravitational waves from first-order cosmological phase transitions: lifetime of the sound wave source

John Ellis^{1,2,3}, Marek Lewicki^{1,4}, José Miguel No^{5,6}

¹Department of Physics, King's College London, Strand, London WC2R 2LS, UK

²Theoretical Physics Department, CERN, Geneva, Switzerland

³National Institute of Chemical Physics & Biophysics, R  vala 10, 10143 Tallinn, Estonia

⁴Faculty of Physics, University of Warsaw, ul. Pasteura 5, 02-093 Warsaw, Poland

⁵Instituto de F  sica Te  rica, IFT-UAM/CSIC, Cantoblanco, 28049 Madrid, Spain

⁶Departamento de F  sica Te  rica, Universidad Aut  noma de Madrid, 28049 Madrid, Spain

E-mail: John.Ellis@cern.ch, Marek.Lewicki@kcl.ac.uk, Josemiguel.no@uam.es

Abstract. We study particle-physics models for a first-order phase transition in the early universe, including models with polynomial potentials both with and without barriers at zero temperature, and Coleman-Weinberg-like models with potentials that are classically scale-invariant. We distinguish three possibilities for the transition - detonations, deflagrations and hybrids - and consider sound waves and turbulent mechanisms for generating gravitational waves during the transitions in these models. We argue that in models without a zero-temperature barrier and in scale-invariant models the period during which sound waves generate gravitational waves lasts only for a fraction of a Hubble time after a generic first-order cosmological phase transition, whereas it may last longer in some models with a zero-temperature barrier that feature severe supercooling. We illustrate the implications of these results for future gravitational-wave experiments.

Contents

1	Introduction	1
2	Review of phase transition dynamics and parameters	3
2.1	Definitions and preliminaries	3
2.2	Hydrodynamics	4
3	Correlation between strength and duration of the phase transition: Thin-wall scenario	7
4	General results for polynomial & Coleman-Weinberg-like potentials	9
4.1	Purely thermal transition: no $T = 0$ potential barrier	9
4.2	Tree-level potential barrier at $T = 0$	11
4.3	Classically scale-invariant Coleman-Weinberg-like potential	13
5	Gravitational wave signals	14
5.1	Energy budget	14
5.2	GW sources	16
5.3	Parameter space scans and results	17
6	Conclusions	21
A	Further aspects of hydrodynamics	23
A.1	Detonations	23
A.2	Deflagrations	24
A.3	Hybrids	25
B	Percolation and successful completion of the transition	26
C	Analytic phase transition parameters	27
C.1	Polynomial with only a thermal barrier	27
C.2	Zero-temperature barrier	28
C.3	Classically scale-invariant potential	28

1 Introduction

Many scenarios for physics beyond the Standard Model (BSM) predict a first-order phase transition in the early universe, around or before the epoch of electroweak symmetry breaking. Studies of such models have long been motivated by the hope of realising electroweak baryogenesis (see, e.g., [1–3]). Another motivation has come to the fore recently, namely that a strong first-order phase transition is also a potential source of gravitational waves (GWs) that could be measured by future detectors (see, e.g., [4] and also [5–7] for recent reviews), allowing a direct probe of the physics of the early Universe before Big-Bang Nucleosynthesis. Specifically, a cosmological first-order phase transition during the radiation-dominated era could, depending on the temperature at which it took place, generate a GW signal at frequencies ~ 10 Hz where LIGO [8] and the future Einstein Telescope (ET) [9] have optimal

detection capabilities, and/or the $0.1 - 1$ Hz frequency band where atom interferometers such as MAGIS [10], AION [11] and AEDGE [12] may offer the best hope of detection, and/or the $10^{-3} - 10^{-2}$ Hz frequency band where space-based laser interferometers such as LISA [13] are most sensitive (see [14] for a recent analysis of the synergies among the various GW detectors). A third motivation for studying BSM scenarios that predict a first-order phase transition in the early universe is the possibility that they might generate a primordial intergalactic magnetic field (see, e.g., [15]).

The above motivations underline the importance of modelling accurately such a first-order cosmological phase transition, and its potential GW signal in particular. This is a non-trivial problem, especially in the interesting case of violent, strong transitions, since there are several mechanisms for generating GWs, involving the interplay between scalar field theory and the hydrodynamics of the primordial plasma. Among the sources of GWs from a first-order phase transition are bubble collisions, sound waves and turbulence in the plasma following the transition. The plasma sound waves that develop after the collisions of bubbles [16–20] have attracted particular attention (see [5, 7] for a review), in view of their distinctive peaked frequency distribution and the fact that they are potentially a long-lasting GW source, which could in general give rise to a sizeable GW signal, and also in view of the difficulties in estimating reliably the strength of the GW signal generated by turbulence in the plasma. Bubble collisions are an easier source to understand theoretically, since it is not necessary to model the plasma. However, it is not easy to realise a transition strong enough for this source to be important in a thermal background (see, e.g., [21]).

A key element in estimating the strength of the GW from sound waves is the duration of the acoustic period during which sound waves may be emitted. Some calculations have been based on estimates that the period of sound wave emission lasts a Hubble time, after which Hubble expansion shuts down the GW source (Hubble damping). However, we have found previously [21, 22] that in specific models this acoustic period lasts significantly less than a Hubble time. In this work we discuss systematically the possible duration of the acoustic period in a variety of particle-physics scenarios featuring a first-order cosmological phase transition, emphasising that the parameters describing the strength and duration of the transition are not independent. We consider generic polynomial potential models with and without zero-temperature barriers, as well as Coleman-Weinberg-like potential models that are almost scale-invariant. We find that the acoustic period is necessarily limited in polynomial models without a zero-temperature barrier, and in Coleman-Weinberg-like models. However, it may extend as long as a Hubble time in polynomial models with a zero-temperature barrier, though only in a restricted range of parameter space. We illustrate the implications of these results for the potential GW signals in the LIGO [8], ET [9], MAGIS [10], AION [11], AEDGE [12] and LISA [13] detectors.

The structure of this paper is as follows. In Section 2 we review the general ingredients to describe a first order phase transition in the early Universe, including in Section 2.2 a discussion of the behaviour of the plasma following the transition, with more details given in Appendix A. In Section 3 we analyse the correlation between the strength and duration of a phase transition in the simple thin-wall approximation. We extend the discussion to generic polynomial potentials and Coleman-Weinberg-like potentials in Section 4. The implications of our results for the GW signals are illustrated in some specific scenarios in Section 5, and we summarise our conclusions in Section 6. Relevant aspects of hydrodynamics, details on the completion of the transition and explicit analytic formulae for parameters of the phase transitions in the models we study are presented in the Appendices.

2 Review of phase transition dynamics and parameters

2.1 Definitions and preliminaries

Our starting point is the decay rate of the false vacuum due to thermal effects [23, 24]:

$$\Gamma \propto T^4 \exp -\frac{S_3(T)}{T}, \quad (2.1)$$

where S_3 is the action for the tunnelling field solution.¹ In the simplest approximation the transition takes place when, on average, one bubble is nucleated in every horizon volume, which defines the transition time (temperature) t_* (T_*):

$$\int_0^{t_*} \frac{\Gamma}{H^3} dt = \int_{T_c}^{T_*} \frac{dT}{T} \frac{\Gamma}{H^4} = 1, \quad (2.2)$$

where in the second equality we only integrate from T_c (the temperature at which the two minima are degenerate) since the decay rate vanishes at earlier times. The next step in studying the phase transition is to obtain Γ as a function of temperature. For a generic scalar field, the action of the tunnelling solution from a false vacuum ϕ_f to a true vacuum ϕ_t , assuming as usual $O(3)$ symmetry, is given by

$$S_3 = 4\pi \int dr r^2 \left(\frac{\dot{\phi}^2}{2} + V(\phi) \right) \quad (2.3)$$

where, in order to find the field profile $\phi = \phi(r)$, one typically has to solve numerically the corresponding equation of motion

$$\ddot{\phi} + \frac{2}{r} \dot{\phi} = \frac{dV}{d\phi} \quad (2.4)$$

with the boundary conditions

$$\dot{\phi}(r=0) = 0, \quad \phi(r \rightarrow \infty) = \phi_f, \quad (2.5)$$

whose profile corresponds to a bubble nucleating in the false vacuum background and reaching beyond the barrier at the origin of our coordinates.

The inverse duration of the phase transition (in Hubble units), β/H , is generally found by Taylor-expanding to first order² the exponent in Eq. (2.1) around t_*

$$\Gamma \propto e^{-\frac{S_3(T)}{T}} = e^{\beta(t_* - t) + \dots}, \quad (2.6)$$

and differentiating both sides of (2.6) with respect to t , which yields

$$\beta = -\frac{d}{dt} \frac{S_3(T)}{T} = H(T) T \frac{d}{dT} \frac{S_3(T)}{T}. \quad (2.7)$$

The strength, α , of a first-order phase transition may be defined as the difference in the trace of the energy-momentum tensor $\theta = (e - 3p)/4$ between the symmetric and broken phases,

¹We refer the reader to [22] for a more detailed discussion.

²Except for very strong supercooling, for which this method breaks down and further terms in the expansion need to be included in the computation of β/H (see [22, 25–27] for details).

normalised to the radiation background energy density in the unbroken phase (see [7] for details), i.e.

$$\alpha(T) \equiv \frac{\Delta\theta}{\rho_R} = \frac{\Delta V(T) - \frac{T}{4} \frac{\partial \Delta V(T)}{\partial T}}{\rho_R}, \quad (2.8)$$

where $\Delta V(T) = V_f - V_t$, with $V_f \equiv V(\phi_f)$ and $V_t \equiv V(\phi_t)$ the values of the potential in the false and true vacua respectively.

Before continuing, we note that the two terms in the action (2.3) are not in fact independent. Based on simple dimensional analysis one can show that for a bubble profile solution they are in fact identical up to a coefficient [28], such that

$$S_3 = 4\pi \int dr r^2 \left(\frac{\dot{\phi}^2}{2} + V(\phi) \right) = \frac{2}{3} \times 4\pi \int dr r^2 \frac{\dot{\phi}^2}{2} = -2 \times 4\pi \int dr r^2 V(\phi), \quad (2.9)$$

where we set $V(\phi_f) = 0$, in which case the integral above is finite. The last equality in (2.9) already points to the fact that the value of β/H , being related to the derivative of the action S_3 , is correlated with the value of α , which is related to the endpoints of the integrand in this last equality.

2.2 Hydrodynamics

We now review the main aspects of the plasma hydrodynamics in the presence of expanding bubbles from a cosmological first-order phase transition, as needed for a description of the various GW sources from the transition (see Section 5). As is customary in phase transition studies, we consider a single expanding bubble interacting with the plasma background and follow the derivation in [29–31] (see also [20]), expanding on it when necessary.

We assume that the thermal plasma can be described as a perfect fluid, with a four-velocity field

$$U_\mu = \frac{(1, \vec{v})}{\sqrt{1 - |\vec{v}|^2}} = (\gamma, \gamma \vec{v}). \quad (2.10)$$

The energy-momentum tensor then reads $T_{\mu\nu} = wU_\mu U_\nu - g_{\mu\nu}p$, where p is the pressure and $w = T(\partial p / \partial T)$ is the enthalpy. We can then use energy-momentum conservation, $\partial_\mu T^{\mu\nu} = 0$, with appropriate boundary conditions, to derive the behaviour of the plasma. The conservation of energy and momentum is non-trivial across the bubble wall, due to the change in the pressure $\Delta p = -\Delta V$ between the two phases. Matching the energy-momentum inside (–) and outside (+) the bubble gives the conditions satisfied at the bubble wall [29]:

$$\frac{w_+ v_+^2}{1 - v_+^2} + p_+ = \frac{w_- v_-^2}{1 - v_-^2} + p_- \quad \text{and} \quad \frac{w_+ v_+}{1 - v_+^2} = \frac{w_- v_-}{1 - v_-^2}, \quad (2.11)$$

where $v = |\vec{v}|$. Assuming a simplified bag-model equation of state,³ we obtain the equation describing the difference in plasma velocities on the two sides of the wall:

$$v_+ = \frac{1}{1 + \alpha_+} \left[\left(\frac{v_-}{2} + \frac{1}{6v_-} \right) \pm \sqrt{\left(\frac{v_-}{2} + \frac{1}{6v_-} \right)^2 + \alpha_+^2 + \frac{2}{3}\alpha_+ - \frac{1}{3}} \right], \quad (2.12)$$

³This simplified model follows from a relativistic gas approximation, and has been shown also to be a good approximation in more realistic conditions [31].

where α_+ is normalised to the radiation energy density immediately in front of the bubble wall, and may not coincide with the strength of the transition obtained from Eq. (2.8) (we elaborate on the connection between the two in Appendix A).

In order to obtain the plasma velocity and enthalpy profiles away from the phase boundary we again use energy-momentum conservation, which gives

$$\partial_\mu T^{\mu\nu} = U^\nu \partial_\mu (U^\mu w) + U^\mu w \partial_\mu U^\nu - \partial^\nu p = 0. \quad (2.13)$$

We consider only spherically-symmetric bubble configurations, such that the fluid spatial dependence is given in terms of the radial coordinate r from the centre of the bubble. Since there are no other relevant scales in the problem apart from the time since nucleation, t , the velocity and enthalpy/temperature profiles exhibit a self-similar behaviour, characterised by the ratio $\xi = r/t$. With these conditions, we obtain from (2.13) differential equations for the velocity profile $v(\xi)$ and enthalpy profile $w(\xi)$ of the plasma

$$\frac{2v}{\xi} = \frac{1 - \xi v}{1 - v^2} \left[\frac{1}{c_s^2} \left(\frac{\xi - v}{1 - \xi v} \right)^2 - 1 \right] \partial_\xi v, \quad (2.14)$$

$$\partial_\xi \omega = 2\omega (c_s^2 + 1) \frac{v}{\xi} \frac{\xi - v}{(\xi - v)^2 - c_s^2 (1 - \xi v)^2}, \quad (2.15)$$

where c_s is the speed of sound in the plasma, given by $c_s^2 = 1/3$ in a relativistic fluid. The appropriate boundary conditions for these equations depend on the terminal velocity v_w that the bubble wall reaches.⁴ As v_w increases, the plasma profile accompanying the expanding bubble may behave in three qualitatively different ways, the so-called *deflagration*, *hybrid* and *detonation* solutions to Eqs. (2.14) and (2.15) [31], whose details we give in Appendix A. From the fluid profiles for $v(\xi)$ and $w(\xi)$ given by these solutions, we can obtain several quantities on which the GW signals from the phase transition depend directly. First, the fraction κ of energy in the fluid converted into bulk fluid motion (i.e., not gone into reheating the plasma), given by [31]

$$\kappa = \frac{3}{\alpha \rho_R v_w^3} \int w \xi^2 \frac{v^2}{1 - v^2} d\xi. \quad (2.16)$$

A related quantity, which will also prove crucial for GW emission, is the root-mean-square (RMS) four-velocity of the plasma \bar{U}_f [17, 19, 20] (see also [7]), defined by

$$\bar{U}_f^2 = \frac{1}{\bar{w} V} \int_V T^{ii} d^3x = \frac{3}{\bar{w} v_w^3} \int w \xi^2 \frac{v^2}{1 - v^2} d\xi, \quad (2.17)$$

where V is the averaging volume and \bar{w} is the average total enthalpy density in the symmetric phase. In the last step of (2.17) we have particularised to a single expanding bubble, but the definition of \bar{U}_f^2 is more general, applicable to a system of many overlapping fluid shells at the end of the phase transition.⁵ Based on the fact that $\bar{w} = \bar{e} + \bar{p}$ (with \bar{p} and \bar{e} , respectively,

⁴In principle this quantity has to be derived from the microphysical description of the interactions between the background scalar field varying across the bubble wall and the thermal plasma in a given particle physics model, see [32–40]. In this work we instead treat v_w as a free parameter, and study the sensitivity to different values.

⁵The results of numerical lattice simulations show that \bar{U}_f^2 from a single expanding bubble very closely matches the results from an ensemble of overlapping bubbles during gravitational wave production at the end of the phase transition [17, 19].

the average pressure and average total energy in the symmetric phase), and thus

$$\bar{w} = (1 + \bar{p}/\bar{e}) \bar{e} = (1 + \bar{p}/\bar{e}) (1 + \alpha) \rho_R \simeq 4/3 (1 + \alpha) \rho_R, \quad (2.18)$$

where in the last step we have used the fact that $p/e = 1/3$ for a relativistic perfect fluid, one obtains a very simple approximation to the RMS fluid velocity [19]

$$\bar{U}_f \simeq \sqrt{\frac{3}{4} \frac{\kappa \alpha}{1 + \alpha}}. \quad (2.19)$$

We show the efficiency κ and RMS fluid velocity for several values of α in Fig. 1, as functions of the wall velocity v_w .

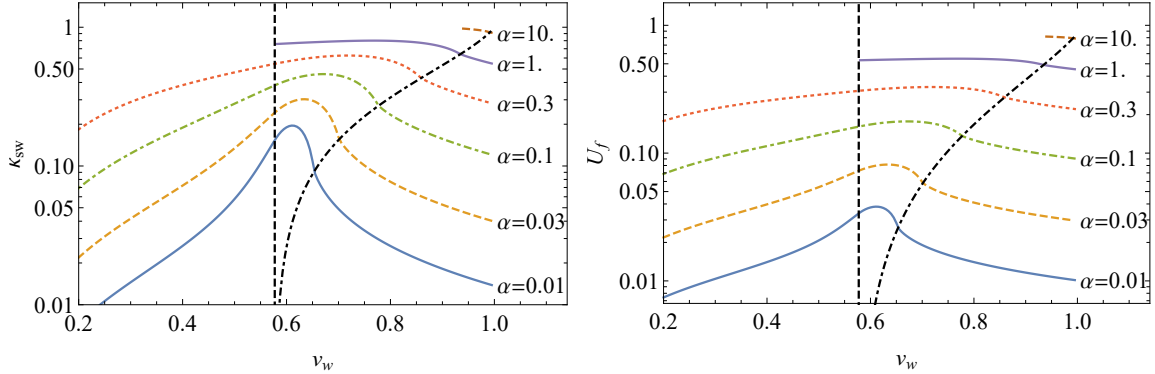


Figure 1: Efficiency of energy transfer into bulk fluid motion κ_{sw} (left panel) and RMS fluid velocity \bar{U}_f (right panel) for a range of transition strengths α as functions of the wall velocity v_w . The black dashed vertical line shows the boundary between deflagration (for $v_w < c_s$) and hybrid (for $v_w > c_s$) fluid profile solutions while the dot-dashed black line show the boundary between deflagration (for $\alpha < \alpha_{\text{det}}^{\text{max}}$) and detonation (for $\alpha > \alpha_{\text{det}}^{\text{max}}$) solutions (see Eq. (A.2) in Appendix A).

At the end of the phase transition, the collisions of the bubbles result in the merging of fluid shells accompanying the respective bubbles, giving rise to a stage of linear fluid evolution (of overlapping fluid shells) after the transition, during which GWs are sourced by the sound waves that develop in the plasma [16–20] (see Section 5). The timescale for shock formation τ_{sh} in the plasma [41] gives the duration of the linear fluid evolution period, after which the GW production from sound waves shuts off [19]. This makes τ_{sh} a key quantity for GW generation, as it determines how long the plasma sound waves are active as a GW source. It can be estimated as [19, 41]

$$\tau_{\text{sh}} \sim L_f / \bar{U}_f, \quad (2.20)$$

where L_f is the characteristic length of the fluid flow. The comparison of τ_{sh} with the Hubble scale allows us to check whether the linear evolution of the fluid flow and the GW sources associated with it can be considered long-lasting ($H \tau_{\text{sh}} \gtrsim 1$), which has a crucial impact on the GW generation from the phase transition and constitutes the main focus of this work.

The characteristic fluid length L_f is in general given approximately by the mean bubble separation at percolation R_* , such that

$$H \tau_{\text{sh}} \sim \frac{H R_*}{\bar{U}_f} \approx \frac{(8\pi)^{\frac{1}{3}} v_w}{\bar{U}_f} \left(\frac{\beta}{H} \right)^{-1}, \quad (2.21)$$

where in the last step we have used the relation between R_* and the duration of the phase transition [42]. Recalling that we need α and v_w to compute \bar{U}_f , it becomes apparent that for a certain bubble wall velocity, we can easily express $H \tau_{\text{sh}}$ as a function of α and $\frac{\beta}{H}$, and so find the boundary between long-lasting ($H \tau_{\text{sh}} \gtrsim 1$) and short-lasting ($H \tau_{\text{sh}} < 1$) plasma sound waves in the $(\alpha, \beta/H)$ parameter space.

3 Correlation between strength and duration of the phase transition: Thin-wall scenario

As already pointed out at the end of Section 2.1, the strength and the duration of a cosmological first-order phase transition are not fully independent parameters, but rather are correlated for particle physics models. Our goal in this work is to discuss generic properties of the phase transition, rather than to study a specific example. From an analytical perspective, we need to make certain approximations in order to do so.

In this Section we discuss the so-called thin-wall limit [43], in which the bubble profile is approximated by just two field values, one inside and the other outside the bubble:

$$\phi_{\text{tw}} = \begin{cases} \phi_{\text{t}} & \text{for } r < R_0, \\ \phi_{\text{f}} & \text{for } r > R_0, \end{cases} \quad (3.1)$$

where R_0 is the radius of the bubble. The key part of this solution is finding the radius of the bubble at nucleation, which turns out to be (see, e.g., [44])

$$R_0 = \frac{3\sigma}{\Delta V}, \quad (3.2)$$

just as in the four-dimensional case where, as usual,

$$\sigma = \int_{\phi_{\text{f}}}^{\phi_{\text{t}}} d\phi \sqrt{2V(\phi) - V_{\text{t}}}, \quad (3.3)$$

and we recall that we set the constant term in the potential such that $V(\phi_{\text{f}}) = 0$ (hence the extra $-V_{\text{t}}$ term in the square root). Using the thin-wall approximation we can simply write the action (2.9) as

$$S_3 = -2 \times 4\pi \int dr r^2 V(\phi) = \frac{4\pi}{3} \times 2R_0^3 \Delta V = \frac{8\pi}{3} \frac{27\sigma^3}{(\Delta V)^2} = 72\sigma^3 \frac{\rho_{\text{r}}^2}{\alpha^2} = \frac{72\sigma^3 T^8}{\alpha^2 \xi_g^4}, \quad (3.4)$$

where $\xi_g = \sqrt{30/\pi^2 g_*}$ and g_* is the number of relativistic degrees of freedom at the time of the phase transition (in the phase ϕ_{f}). In potentials where the thin-wall solution is a good approximation, ΔV is only a small correction term in the potential. This means that σ is modified by only a negligible additive constant when α changes. Thus, in order to compute β from (3.4) we need to include only the explicit polynomial dependence on the temperature, which implies

$$\frac{\beta}{H} = T \frac{d}{dT} \frac{S_3}{T} \propto \frac{S_3}{T} \propto \alpha^{-2}, \quad (3.5)$$

yielding a simple polynomial dependence of β/H on α . Remembering also that the Hubble expansion rate is

$$H^2 = \frac{1}{3M_p^2} (\rho_{\text{R}} + \rho_{\text{V}}) = \frac{1}{3M_p^2} \left(\frac{T^4}{\xi_g^2} + \Delta V \right), \quad (3.6)$$

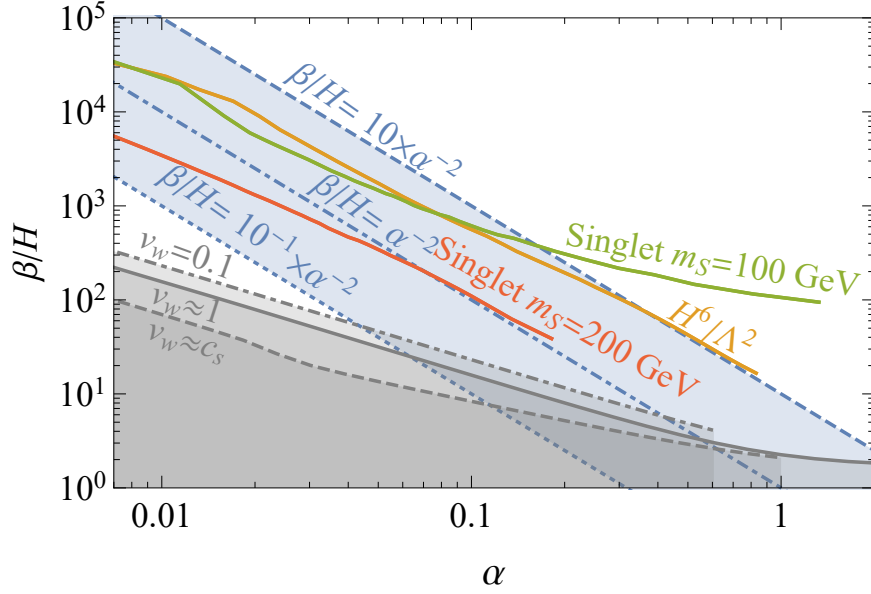


Figure 2: β/H as a function of α for the simple thin-wall approximation, with the multiplicative constant (see text for details) set to 10 (dotted blue), 1 (dot-dashed blue) and 0.1 (dashed blue). Also shown are the numerical results for a singlet scalar extension of the SM with the singlet mass $m_s = 100$ GeV (solid green) and $m_s = 200$ GeV (solid red), as well as for the SM extended by a non-renormalizable term $\propto H^6$ (solid yellow). The grey regions correspond to $H\tau_{\text{sh}} > 1$ for different values of the bubble wall velocity.

we can rewrite the nucleation condition (2.2) as

$$1 \approx \frac{\Gamma}{H^4} \implies \frac{S_3}{T} \approx -\log\left(\frac{1}{9M_p^4} \frac{T^4}{\xi_g^4}\right) \approx 167 - 4\log(T/\text{GeV}), \quad (3.7)$$

where we have fixed for simplicity $g_* = 100$ (approximating the number of relativistic d.o.f. in the early Universe around the electroweak scale). Eq. (3.7) allows us to fix the value of S_3/T and consequently β/H at the nucleation temperature. However we must still find the value of α at that reference temperature, so this simplified approach only yields the value of β/H as a function of α up to a multiplicative constant.

The results for the dependence of β/H on α in the thin-wall limit for several values of the unknown multiplicative constant are shown in Fig. 2. For comparison we also show realistic results from two BSM scenarios, namely the SM extended with an H^6 non-renormalizable operator and the singlet scalar extension of the SM (details can be found in [21, 22]). As shown in Fig. 2, the simple thin-wall approximation captures reasonably well the trend found in realistic scenarios. Fig. 2 also shows the approximate location of the boundary $H\tau_{\text{sh}} = 1$ between short- and long-lasting plasma sound waves, for different values of the bubble wall velocity v_w up to the maximum value of α allowed for each value of v_w . The results from Fig. 2 already indicate that for weaker phase transitions (smaller α) the lifetime of the sound wave GW source compared to a Hubble time is in general shorter. At the same time, the long-lifetime region $H\tau_{\text{sh}} \gtrsim 1$ is approached only for very strong transitions (particularly if

$(\beta/H)\alpha^2 > 1$ in the thin-wall approximation). In the next Section we analyze this in more detail away from the thin-wall limit.

4 General results for polynomial & Coleman-Weinberg-like potentials

We now analyze the possible lifetime of the sound-wave source for some generic scalar potentials. We first study the case of a polynomial potential without a potential barrier between the false and true vacua at $T = 0$, corresponding to a purely thermal phase transition. Then we investigate the case of a polynomial potential with a non-zero barrier at $T = 0$, and finally the case of a Coleman-Weinberg-like (classically scale-invariant) potential. In the latter two cases, significant supercooling during the phase transitions is possible, which could lead to a breakdown of the relation $\Gamma \propto e^{-\beta t}$ from Eq. ((2.6)). This is typically the case for slow phase transitions, with $\beta/H \lesssim 10$. In order to deal with this problem in our analysis, throughout this work we use the refined analysis of percolation and phase transition completion described in detail in [22] and discussed here in Appendix B.

4.1 Purely thermal transition: no $T = 0$ potential barrier

We consider first the simplest renormalisable scalar potential, which takes the form

$$V = m^2 \phi^2 - a \phi^3 + \lambda \phi^4, \quad (4.1)$$

where λ , a and m^2 are parameters that may in general depend on the temperature T . For this simple potential, there is an accurate semi-analytical approximation to the tunnelling action [45]:

$$\frac{S_3}{T} = \frac{a}{T\lambda^{3/2}} \frac{8\pi\sqrt{\delta}(\beta_1\delta + \beta_2\delta^2 + \beta_3\delta^3)}{81(2-\delta)^2}, \quad \text{where } \delta \equiv \frac{8\lambda m^2}{a^2}, \quad (4.2)$$

with $\beta_1 = 8.2938$, $\beta_2 = -5.5330$ and $\beta_3 = 0.8180$.

Using the high-temperature expansion for the 1-loop finite-temperature effective potential (see [46] for details), we can use the simple potential from (4.1) to approximate realistic particle physics scalar potentials:

$$V(\phi, T) = \frac{g_{m^2}}{24} (T^2 - T_0^2) \phi^2 - \frac{g_m}{12\pi} T \phi^3 + \lambda \phi^4, \quad (4.3)$$

where we consider $T_0^2 > 0$, in which case T_0 corresponds to the temperature below which the potential barrier disappears and the false vacuum $\phi_f = 0$ becomes unstable. This results in a purely thermal phase transition.

For realistic particle physics models, the dimensionless constant g_{m^2} in (4.3) is related to the squared-mass shifts at the bubble wall for all the particles coupled to ϕ , due to the change in vacuum expectation value $\Delta\phi$ across the phase boundary. This corresponds to the number of degrees of freedom coupled to ϕ weighted by their couplings squared (g_f for fermions and g_b for bosons). The interpretation of g_m is similar except that now only linear mass shifts in bosonic degrees of freedom contribute, weighted by their couplings g_b squared:

$$\begin{aligned} g_{m^2} &\equiv \frac{1}{(\Delta\phi)^2} \left(\sum_b N_b \Delta m_b^2 + \frac{1}{2} \sum_f N_f \Delta m_f^2 \right) = \sum_b N_b g_b^2 + \frac{1}{2} \sum_f N_f g_f^2. \\ g_m &\equiv \frac{1}{\Delta\phi} \left(\sum_b N_b g_b^2 \Delta m_b \right) = \sum_b N_b g_b^3. \end{aligned} \quad (4.4)$$

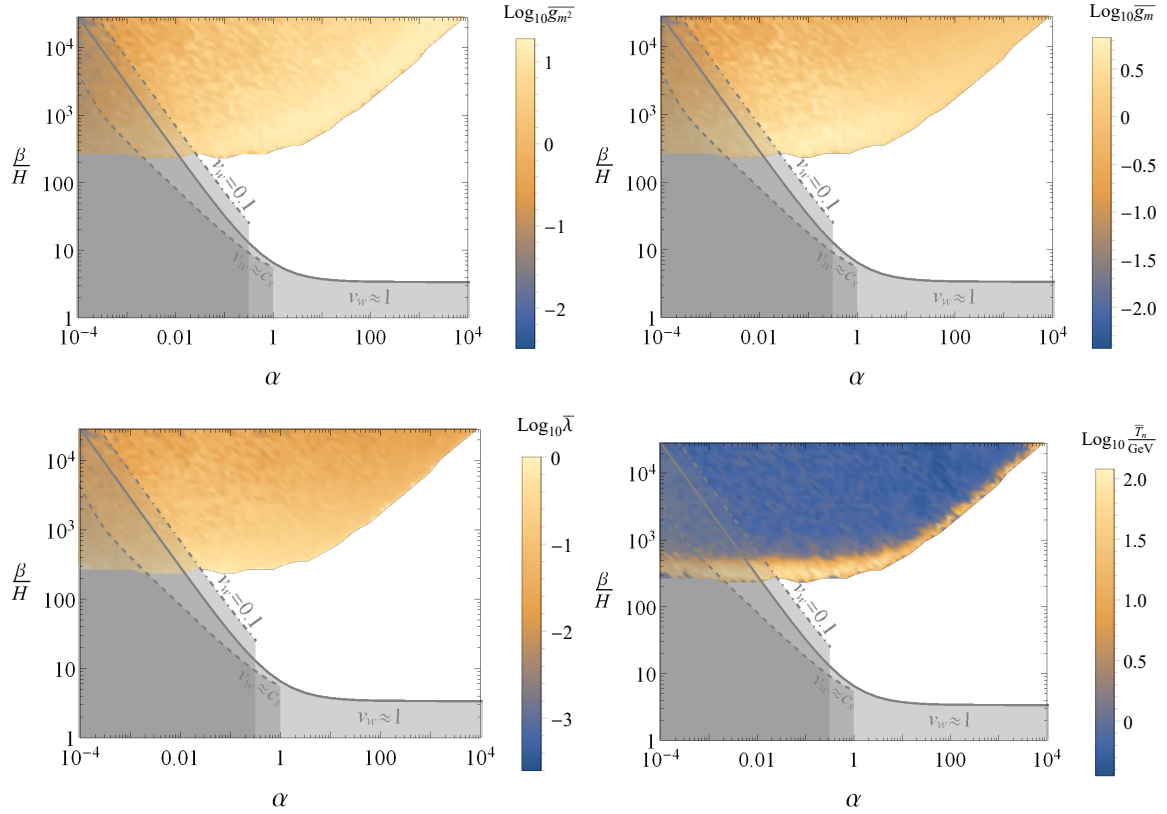


Figure 3: Regions of the $(\alpha, \beta/H)$ plane realised for the polynomial potential with a purely thermal barrier, Eq. (4.3). The colour shading indicates the geometric average of the scan for the values of g_{m^2} (upper left), g_m (upper right) and λ (lower left) in the potential (4.3), as well as the nucleation temperature T_n (lower right) for each point in the plane. The grey shading indicates the regions with long-lived sound-wave emission for different bubble wall velocities.

Combining (4.3) with (4.2) and (4.1), after some algebra we can express the α and β/H parameters as simple analytical functions. The explicit results are a bit lengthy and we show them in Appendix C. Our analysis then consists of finding the percolation temperature as described in Appendix B and using the explicit results from Appendix C to obtain the key transition parameters at percolation. This remarkable simplification, compared to the standard search for a bounce solution, allows us to perform a simple scan over the parameter space to show the landscape of possible results, shown explicitly in Fig. 3. The ranges chosen for the parameter scan (with a logarithmic prior) are

$$\begin{aligned}
 10^{-4} &\leq g_{m^2} \leq 10^2, \\
 10^{-4} &\leq g_m \leq g_{m^2}, \\
 10^{-6} &\leq \lambda \leq 10, \\
 10^{-3} \text{ GeV} &\leq T_0 \leq 10^5 \text{ GeV}.
 \end{aligned}
 \tag{4.5}$$

Our chosen scan upper limit for g_{m^2} is motivated from (4.4), by considering $N_b + N_f/2 \lesssim 100$ and $g_b, g_f \lesssim 1$. We stress that close to these boundaries perturbation theory ceases to be

reliable, and our results should there be interpreted as indicative at best. The condition $g_m < g_{m^2}$ in our scan is also motivated by requiring $g_b, g_f \lesssim 1$ (recall Eq. (4.4)).

We have verified the accuracy of our scanning method by comparing the results obtained for a subset of points in the scan against a full calculation based on finding the bounce solution (as explained e.g. in [21, 22]), finding very good agreement for all the verified points (the difference comes mostly from approximating the transition temperature by the nucleation temperature instead of the percolation temperature). We have also verified the fit to the bounce action given in [45].⁶

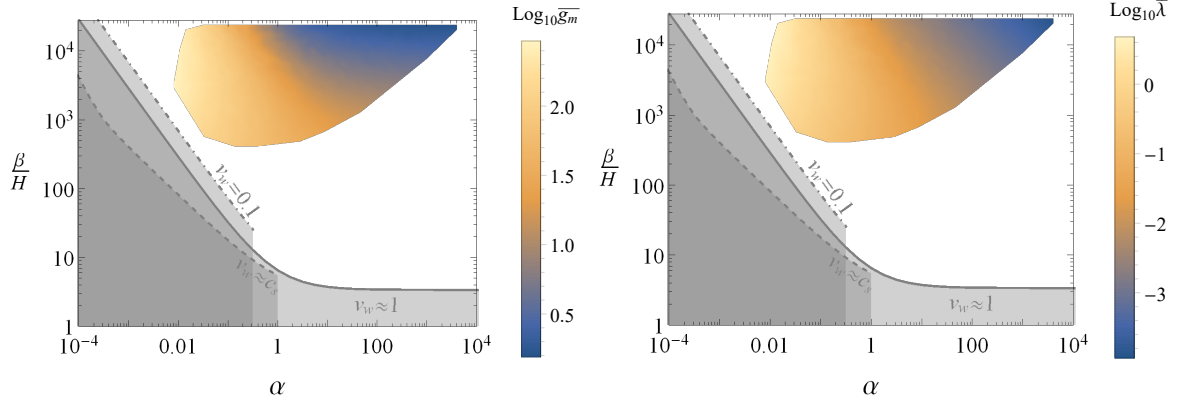


Figure 4: Regions of the $(\alpha, \beta/H)$ plane realised for the polynomial potential with a purely thermal barrier, Eq. (4.3), for fixed $g_{m^2} = 100$ and $T_0 = 100$ GeV. The colour shading indicates the geometric average of the scan for the values of g_m (left) and λ (right) for each point in the plane. The grey shading indicates the regions with long-lived sound-wave emission for different bubble wall velocities.

From the results in Fig. 3 we see immediately that there exists an approximate lower bound on the value of β/H (whose specific value depends on the upper and lower limits of the scan parameters g_{m^2}, g_m and λ) when the transition is purely thermal and the potential barrier between vacua disappears at some finite temperature T_0 . At the same time, Fig. 3 shows that transition strength values $\alpha \gg 1$ are compatible with successful percolation even in this case, provided that the nucleation rate is fast enough, which is possible in regions of the parameter space where β/H is sufficiently large. This happens for large values of g_{m^2} together with very small values of both g_m and λ in (4.3), as shown in Fig. 4. However, we note that in this corner of the parameter space the potential (4.3) is not expected to capture well the behaviour of realistic particle physics models: Eq. (4.3) neglects both thermal and quantum corrections to λ , and it is precisely for very small tree-level values of λ that they become important, increasing the overall size of the quartic term in Eq. (4.3) (and adding a temperature dependence to it). As a result, large values of α in scenarios with a purely thermal potential barrier between vacua are very difficult to obtain in general.

4.2 Tree-level potential barrier at $T = 0$

We turn in this Section to the discussion of polynomial potentials with a barrier between vacua that persists down to $T = 0$. In comparison to the analysis of the previous Section,

⁶Specifically, while in any particular transition the values of β_i parameters in (4.2) can change slightly, this has a negligible impact on the resulting nucleation or percolation temperature, as well as on α and β/H .

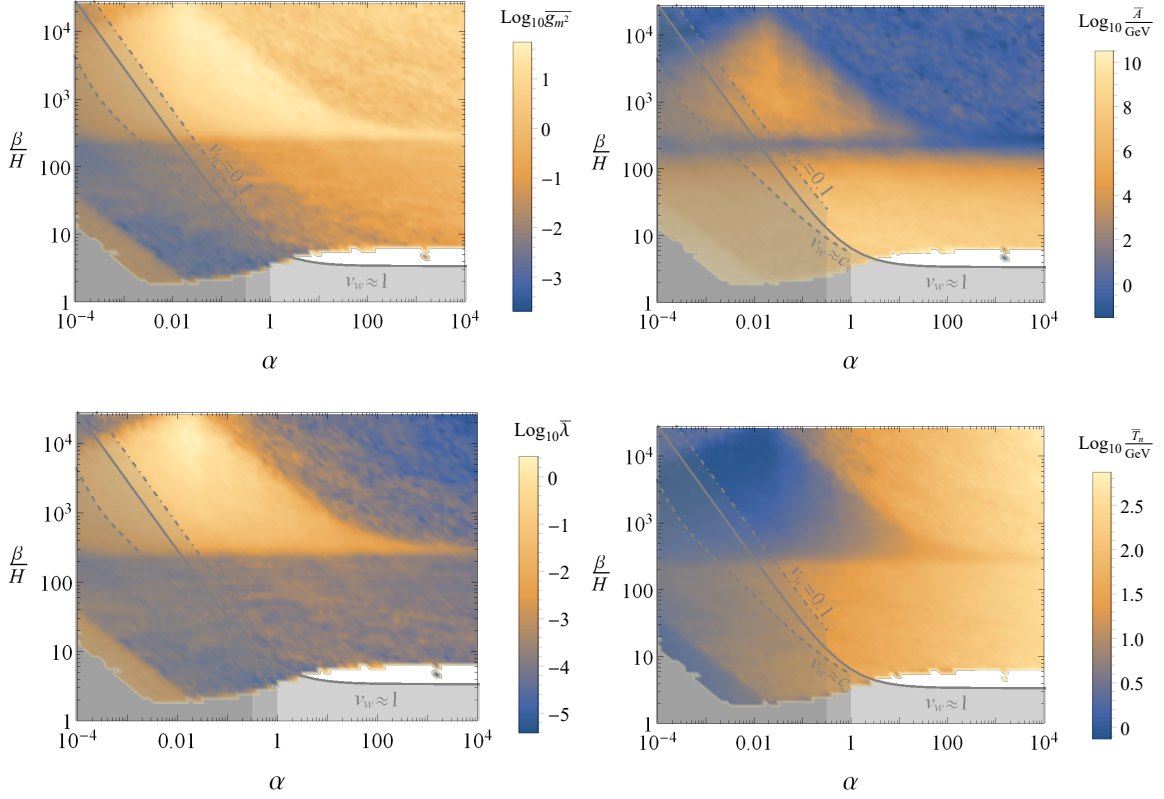


Figure 5: Allowed regions of the $(\alpha, \beta/H)$ plane for the potential (4.6). The colour shading indicates the geometric average of the values of g_m^2 (upper left), A/GeV (upper right) and λ (lower left) in the potential (4.6), as well as the nucleation temperature T_n/GeV (lower right) for each point in the plane. The grey shading indicates the regions with long-lived sound-waves for different bubble wall velocities.

we now introduce a potential barrier at tree-level via a term $A\phi^3$, and for simplicity assume that it dominates over the thermal cubic term in (4.3), $A \gg g_m T_0$, so that we can neglect the latter. The resulting scalar potential reads

$$V(\phi, T) = \frac{g_m^2}{24} (T^2 - T_0^2) \phi^2 - A\phi^3 + \lambda\phi^4, \quad (4.6)$$

where we again relate g_m^2 to the mass shifts across the bubble wall, see (4.4). Also, now $T_0^2 < 0$ is allowed so that the false vacuum $\phi_f = 0$ can persist as a (local) minimum down to $T = 0$. Combining (4.2) and (4.6) we can express the parameters α and β/H in analytical form, as shown explicitly in Appendix C.2. We again perform a scan over the parameter space, within the ranges

$$\begin{aligned} 10^{-6} &\leq g_m^2 \leq 10^2, \\ 10^{-3} \text{ GeV} &\leq A \leq 10^{10} \text{ GeV}, \\ 10^{-8} &\leq \lambda \leq 10, \\ 10^{-3} \text{ GeV} &\leq T_0 \leq 10^5 \text{ GeV} \end{aligned} \quad (4.7)$$

also considering for each point both signs for T_0^2 in (4.6). We show the results in Fig. 5.

Compared to the results of Section 4.1, in this case there is a broader range of the parameter space that may yield long-lived sound waves as a source of GWs, particularly since now low values of β/H of $\mathcal{O}(10 - 100)$ become possible. Despite the fact that some of the results predict very low β/H , we emphasise again that for each of the points percolation has been verified following the prescription in Appendix B. At the same time, the average bubble size R_* in each of those cases proves to be significantly below the horizon size, even though a naive exponential nucleation prescription would suggest the contrary. Similarly to the case of a purely thermal potential barrier studied in the previous Section, at very low values of λ below $10^{-4} - 10^{-5}$, the potential (4.6) ceases to yield a good approximation to realistic scenarios, for which quantum and thermal corrections to λ would be important in such regime.⁷ From the upper left panel of Fig. 5, we also infer that sound waves with a lifetime longer than a Hubble time tend to have small values of g_{m^2} , so as to create a large hierarchy between the potential squared-mass parameter $\mu^2 \equiv (g_{m^2}/24) \times T_0^2$ and the squared-temperature T_0^2 .

4.3 Classically scale-invariant Coleman-Weinberg-like potential

We turn finally to a very different class of potentials arising in many extensions of the SM, namely (almost) scale-invariant Coleman-Weinberg-like potentials. A generic such potential can be written as [45]

$$V(\phi, T) = (2B_1 - B_2) \sigma^2 T^2 - B_1 \phi^4 + B_2 \phi^4 \log\left(\frac{\phi}{\sigma}\right). \quad (4.8)$$

We again use an analytical approximation to the tunnelling action [45]:

$$\frac{S_3}{T} = \frac{16\pi\sigma I^3}{3T(1-2\delta)^2} \sqrt{\frac{2}{B_2}} (2\delta)^{n_\mu} (1 + \mu_1\delta + \mu_2\delta^2 + \mu_3\delta^3), \quad \delta = \frac{2B_1 - B_2}{2B_2}, \quad (4.9)$$

where $I = 0.4199$, $n_\mu = 0.557$, $\mu_1 = 4.27$, $\mu_2 = -14.59$ and $\mu_3 = 12.09$. We set

$$B_1 = \frac{1}{2} \left(\frac{g^2 T^2}{\sigma^2} + \frac{3g^4}{4\pi^2} \right), \quad B_2 = \frac{3g^4}{4\pi^2}, \quad \sigma = v, \quad (4.10)$$

so that

$$V(\phi, T) = g^2 T^2 \phi^2 + \frac{3g^4}{4\pi^2} \phi^4 \left(\log\left(\frac{\phi^2}{v^2}\right) - \frac{1}{2} - \frac{g^2 T^2}{2v^2} \right), \quad \delta = \frac{2\pi^2 T^2}{3g^2 v^2}, \quad (4.11)$$

which is a reasonable approximation for potentials encountered in particle physics models featuring scale invariance (e.g., the $U(1)_{B-L}$ model studied in [21]). We have again found analytical formulae for the phase transition parameters, the explicit results shown in Appendix C.3. In this scenario there are only 2 free parameters, namely the coupling g and the $T = 0$ scalar field vacuum expectation value v , which simply sets the scale of new physics for the model in question. We perform a scan over them within the ranges

$$10^{-8} < g < 10, \quad 10^{-5} < v/\text{GeV} < 10^{15}, \quad (4.12)$$

in order to explore the available parameter space. The results are shown in Fig. 6. Within the allowed $(\alpha, \beta/H)$ region, we observe that decreasing values of β/H are correlated with

⁷As a result, the blue regions in Fig. 5 (lower left panel) should be interpreted as only indicative.

smaller values of g and larger scales v . Values of g similar to those in the SM lie well within the range of the scan, and give predictions for α and β/H clearly outside the region where sound waves are long-lived. The same is true for all values of v between $\mathcal{O}(\text{GeV})$ and a typical GUT scale. Altogether, Fig. 6 highlights that for scale-invariant Coleman-Weinberg-like scalar potentials the sound wave GW source is only active for a small fraction of a Hubble time.

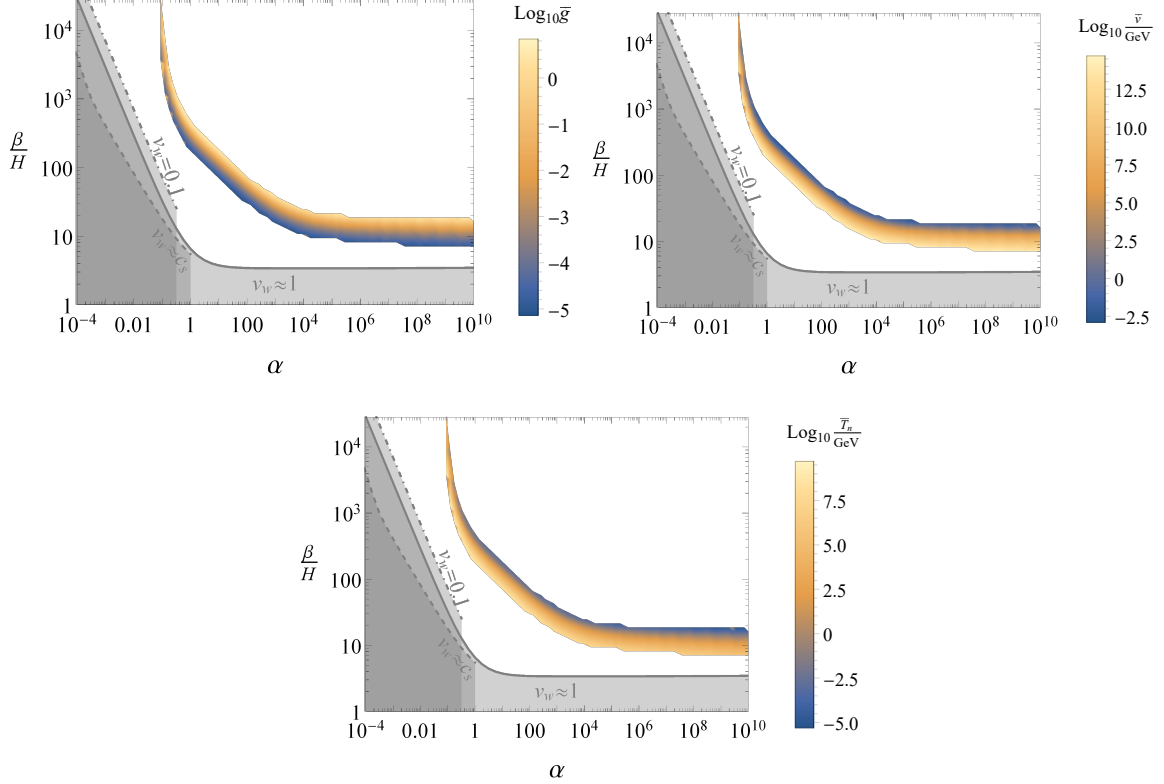


Figure 6: Allowed regions of the $(\alpha, \beta/H)$ plane for scale-invariant Coleman-Weinberg-like scalar potentials like (4.11). The colour shading indicates the geometric average of the values of g (upper left) and v/GeV (upper right), as well as the nucleation temperature T_n/GeV (lower right) for each point in the plane. The grey shading indicates the regions with long-lived sound-waves for different bubble wall velocities.

5 Gravitational wave signals

5.1 Energy budget

We now review the energy budget of the phase transition [31] (see also [21]), in order to discuss the implications of the results from the previous Sections for the production of GWs at the end of the phase transition. First, to compute the fraction of the energy used to accelerate the bubble walls we need the friction acting on the wall, which may be conveniently expressed through the parameters α_∞ and α_{eq} , see [21]. In the case of a purely thermal transition, both

α_∞ and α_{eq} depend directly on the parameters of our scan, and may be readily expressed as:

$$\begin{aligned}\alpha_\infty &= \frac{\Delta m^2 T^2}{24 \rho_R} = \frac{1}{24 \frac{\pi^2}{30} g_*} \left(\frac{\Delta \phi}{T} \right)^2 g_{m^2}, \\ \alpha_{\text{eq}} &= \frac{g^2 \Delta m_V T^3}{\rho_R} \sim \frac{1}{\frac{\pi^2}{30} g_*} \frac{\Delta \phi}{T} g_m.\end{aligned}\tag{5.1}$$

We note that we have conservatively assumed in (5.1) that all bosons (as included in g_m) contribute to α_{eq} , whereas in practice only gauge bosons do [47] so the value of α_{eq} may also be somewhat smaller. The expressions in (5.1) also apply to the tree-level $T = 0$ potential barrier scenario discussed in Section 4.2, though in that case our scan does not include g_m . In the following we assume for definiteness a value $g_m \sim 0.1 g_{m^2}$ (to emulate the suppression w.r.t. g_{m^2} from the lack of fermion contributions together with an additional power of the appropriate coupling) when discussing GW production in this scenario (bearing in mind that a departure of g_m from this value would influence our GW results). Finally, in the scale-invariant Coleman-Weinberg-like scenario discussed in Section 4.3, α_∞ can be directly obtained from the parameters g and v , and we assume the minimal value of α_{eq} given by a model of $U(1)_{B-L}$ gauge symmetry breaking (see e.g. [21]). A summary of the expressions for α_∞ and α_{eq} for the three generic types of phase transitions is given in Table 1.

Model	α_∞	α_{eq}
Thermal barrier	$\frac{5 g_{m^2}}{4 \pi^2 g_*} \left(\frac{\Delta \phi}{T} \right)^2$	$\frac{30 g_m}{\pi^2 g_*} \left(\frac{\Delta \phi}{T} \right)$
Zero-temperature barrier	$\frac{5 g_{m^2}}{4 \pi^2 g_*} \left(\frac{\Delta \phi}{T} \right)^2$	$\frac{30 g_m}{\pi^2 g_*} \left(\frac{\Delta \phi}{T} \right)$
Scale-invariant (CW-like)	$\frac{15 g^2}{\pi^4 g_*} \left(\frac{v}{T} \right)^2$	$\frac{180 g^3}{\pi^3 g_*} \left(\frac{v}{T} \right)$

Table 1: Expressions for α_∞ and α_{eq} in the scenarios from Sections 4.1 (top), 4.2 (middle) and 4.3 (bottom).

Under the assumption that the transition strength satisfies $\alpha > \alpha_\infty$ (the case in which the bubbles undergo an accelerated expansion for part of the phase transition [31, 48]), the γ_{eq} factor the bubble wall reaches when it ceases to accelerate is given by

$$\gamma_{\text{eq}} = \frac{\alpha - \alpha_\infty}{\alpha_{\text{eq}}}.\tag{5.2}$$

The γ factor that the wall would reach at the time of bubble collisions in the absence of plasma friction is simply expressed through the initial and final bubble radii as

$$\gamma_* = \frac{2 R_*}{3 R_0}, \quad H R_* = v_w (8\pi)^{\frac{1}{3}} \left(\frac{\beta}{H} \right)^{-1}, \quad R_0 = \left(\frac{3 S_3}{2 \pi \Delta V} \right)^{\frac{1}{3}},\tag{5.3}$$

where we have already expressed these conveniently through the known action and nucleation rate. The fraction of energy available to produce GWs from bubble collisions is then given by [21]:

$$\kappa_{\text{col}} \approx \frac{3}{2} \frac{\gamma_{\text{eq}}}{\gamma_*}.\tag{5.4}$$

The energy fraction released by the phase transition that is converted into bulk fluid motion [31] has already been given in (2.16), which for $\alpha > \alpha_\infty$ needs to be modified to subtract the energy going into acceleration of the wall instead of the plasma. In the limit of very relativistic walls $v_w \rightarrow 1$ (as expected for $\alpha > \alpha_\infty$), the relevant energy fraction for sound waves reads (see [21, 31])

$$\kappa_{\text{sw}}|_{v_w \rightarrow 1} = \frac{\alpha_{\text{eff}}}{\alpha} \frac{\alpha_{\text{eff}}}{0.73 + 0.083\sqrt{\alpha_{\text{eff}}} + \alpha_{\text{eff}}}, \quad \alpha_{\text{eff}} = \alpha(1 - \kappa_{\text{col}}). \quad (5.5)$$

Finally, in order to obtain the GW spectrum from the phase transition as it would be observed today, we must include the corresponding redshift factors [49]. The normalized energy density scales as:

$$\Omega_{\text{GW},0} = \left(\frac{a_*}{a_0}\right)^4 \left(\frac{H_*}{H_0}\right)^2 \Omega_{\text{GW},*} = 1.67 \times 10^{-5} h^{-2} \left(\frac{100}{g_{\text{eff}}(T_{\text{reh}})}\right)^{\frac{1}{3}} \Omega_{\text{GW},*}, \quad (5.6)$$

while the frequency becomes:

$$f_0 = \frac{a_*}{a_0} f_* = 1.65 \times 10^{-5} \text{ Hz} \left(\frac{T_{\text{reh}}}{100 \text{ GeV}}\right) \left(\frac{g_{\text{eff}}(T_{\text{reh}})}{100}\right)^{\frac{1}{6}} \left(\frac{f_*}{H_*}\right), \quad (5.7)$$

where the star index denotes quantities at the end of the phase transition. The reheating temperature is approximately given by [22]

$$T_n (1 + \alpha)^{\frac{1}{4}}, \quad (5.8)$$

and can be quite different from the temperature at which the phase transition begins, T_n , particularly for very strong transitions where a lot of energy is stored in the form of vacuum energy that later reheats the universe when the transition ends.

5.2 GW sources

We now discuss the GW spectrum generated from sound waves and turbulence in the plasma, as well as from the collisions of scalar field bubbles. We start with the contribution to the GW signal from bubble collisions, as given approximately by [27]:

$$\Omega_{\text{col},*} = 0.3 v_w^2 \left(\frac{\beta}{H}\right)^{-2} \left(\frac{\kappa_{\text{col}} \alpha}{1 + \alpha}\right)^2 \left(\frac{f_*}{f_{\text{col}}}\right)^3 \left[1 + 2 \left(\frac{f_*}{f_{\text{col}}}\right)^{2.07}\right]^{-2.18}, \quad (5.9)$$

with the peak frequency f_{col} given by (we suppress the star index in β/H to match common notation)

$$\frac{f_{\text{col}}}{H_*} \simeq \frac{1.1}{v_w} \frac{\beta}{H}. \quad (5.10)$$

We turn next to GW sources related to the thermal plasma. Using the results from numerical lattice simulations [16, 17, 19], the GW spectrum generated by sound waves propagating in the plasma after the transition may be approximated by [5] (see also [7]):

$$\Omega_{\text{sw},*} = 0.25 v_w (H_* \tau_{\text{sw}}) \left(\frac{\beta}{H}\right)^{-1} \left(\frac{\kappa_{\text{sw}} \alpha}{1 + \alpha}\right)^2 \left(\frac{f_*}{f_{\text{sw}}}\right)^3 \left[1 + \frac{3}{4} \left(\frac{f_*}{f_{\text{sw}}}\right)^2\right]^{-\frac{7}{2}}, \quad (5.11)$$

with the peak frequency given by

$$\frac{f_{\text{sw}}}{H_*} \simeq \frac{1.16}{v_w} \frac{\beta}{H}, \quad (5.12)$$

and the duration of the sound-wave period

$$H_* \tau_{\text{sw}} \equiv \min[1, H_* \tau_{\text{sh}}] \quad (5.13)$$

with $H_* \tau_{\text{sh}}$ given by (2.21). We nevertheless note that a recent analytical description of plasma sound waves [20] yields somewhat different asymptotic behaviours when $f_* \gg f_{\text{sw}}$ and $f_* \ll f_{\text{sw}}$ from that in (5.11). We also stress that the numerical lattice simulations of GW production from plasma sound waves have been carried out for small/moderate values of α , and that the naive extrapolation to scenarios with large phase transition strengths used in this work (e.g., in the scale-invariant Coleman-Weinberg-like case) may not apply (see the discussion in [7]). These comments highlight the fact that the precise understanding of GW production from sound waves is still ongoing, and in that some care must be taken in interpreting our sound wave GW results.

If the sound-wave period lasts much less than a Hubble time, $H_* \tau_{\text{sh}} \ll 1$, there is a sizeable amount of energy in the bulk fluid motion when the flow becomes nonlinear. This energy could then (ideally) be available to create turbulence in the plasma, which also sources GWs. Assuming that all the energy in the bulk fluid motion remaining at the end of the sound wave period is transferred into turbulence, its contribution to the GW spectrum may be modelled as [50]:

$$\Omega_{\text{turb},*} = 19.9 v_w \left(\frac{\beta}{H} \right)^{-1} (1 - H_* \tau_{\text{sw}}) \left(\frac{\kappa_{\text{sw}} \alpha}{1 + \alpha} \right)^{3/2} \frac{\left(\frac{f_*}{f_{\text{turb}}} \right)^3 \left[1 + \left(\frac{f_*}{f_{\text{turb}}} \right) \right]^{-\frac{11}{3}}}{1 + 8\pi f_*/H_*}, \quad (5.14)$$

with the peak frequency

$$\frac{f_{\text{turb}}}{H_*} \simeq \frac{1.75}{v_w} \left(\frac{\beta}{H} \right). \quad (5.15)$$

Given that (5.14) assumes a perfect conversion of bulk fluid energy into turbulent energy, it may be viewed as an upper bound on the possible turbulent GW contribution, assuming a correct modelling of the turbulence as a GW source. In particular, this estimate neglects the possibility that some of that fluid energy is instead converted to plasma heat. It also does not take into account the recent studies on plasma vortical motion at the end of the phase transition [51]. These indicate that for slow deflagrations with sizable α , plasma turbulence can be efficiently generated together with sound waves during the linear evolution of the fluid, and also suggest that the conversion efficiency of vortical energy into GWs is significantly smaller than that of sound waves. All these aspects should be kept in mind when interpreting our results for GWs from turbulence.

5.3 Parameter space scans and results

We have performed scans over the parameter spaces of the three scenarios discussed in Section 4, using the ranges defined there for each of them. The scans have been done separately for three proposed experiments: LISA [13, 52], the Einstein Telescope (ET) [9, 53] and AEDGE [12], using in each case a Monte Carlo Markov chain aimed at maximizing the signal-to-noise ratio (SNR) for a given GW experiment, by varying the parameters a hundred times around initial scan point values.

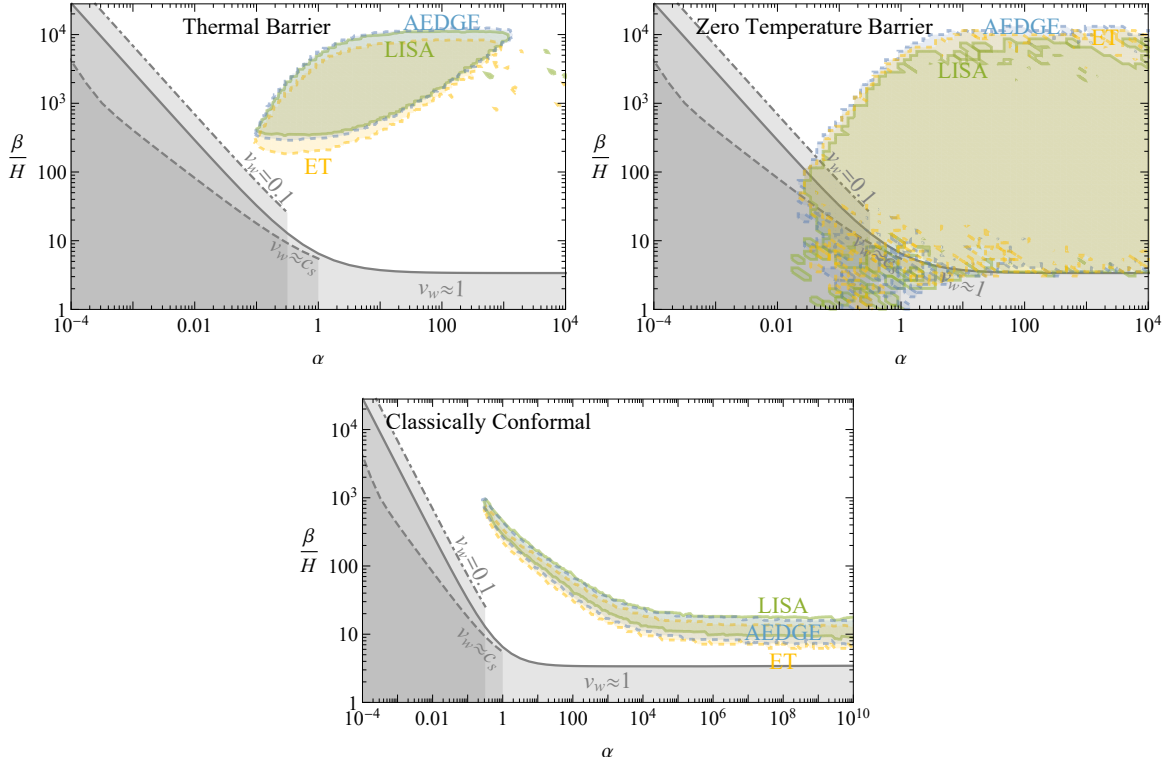


Figure 7: The coloured shading shows the regions of the $(\alpha, \beta/H)$ plane featuring a $\text{SNR} > 10$ for LISA [13, 52] (green), the Einstein Telescope (ET) [9, 53] (orange) and AEDGE [12] (blue), for potential with a pure thermal barrier (upper left), a zero-temperature barrier (upper right) and a scale-invariant Coleman-Weinberg scenario (lower). The grey shading shows the regions with long-lived GW emission from sound waves ($H\tau_{\text{sh}} > 1$) for different bubble wall velocities.

The results of these scans are shown in Fig. 7 as coloured areas in the $(\alpha, \beta/H)$ planes satisfying $\text{SNR} \geq 10$ for LISA (green), ET (orange) and AEDGE (blue), respectively, for the scalar potential with a pure thermal barrier from Section 4.1 (upper left), the scalar potential with a zero-temperature barrier from Section 4.2 (upper right) and the scale-invariant Coleman-Weinberg potential from Section 4.3 (lower). In all the scans we have assumed $v_w \sim 1$ when computing the resulting GW signal, which corresponds to the most optimistic choice for GW production.⁸ We stress that, despite Fig. 7 giving the naive impression that the sensitivity ranges of the GW experiments LISA, ET and AEDGE are fairly similar, this is the case only for β/H and α , but not for the temperature of the transition T_* , which determines the characteristic frequency of the GW signal.

As shown in the upper left panel of Fig. 7, the case of a purely thermal barrier does not allow sound waves to last a significant fraction of a Hubble time. In contrast, for the scenario with a zero-temperature barrier (upper right panel) this is possible for low values of β/H and moderate to large α . It is also important to note that for such supercooled transitions we

⁸We note that Fig. 7 shows the regions where sound waves are long-lasting ($H\tau_{\text{sh}} > 1$) for various values of v_w . Whilst smaller values of v_w increase the β/H range of long-lasting sound waves (for a given α), decreasing v_w would also significantly diminish the amplitude of the resulting GW signal.

always have $\alpha > \alpha_\infty$, so that $v_w \rightarrow 1$ is indeed expected in those cases. Finally, in the lower panel of Fig. 7 we see that in scale-invariant Coleman-Weinberg-like models there is only a restricted band of the $(\alpha, \beta/H)$ plane where GW signals with $\text{SNR} > 10$ can be achieved which, as already shown in Section 4.3, lies well within the region where sound waves only last for a small fraction of a Hubble time.

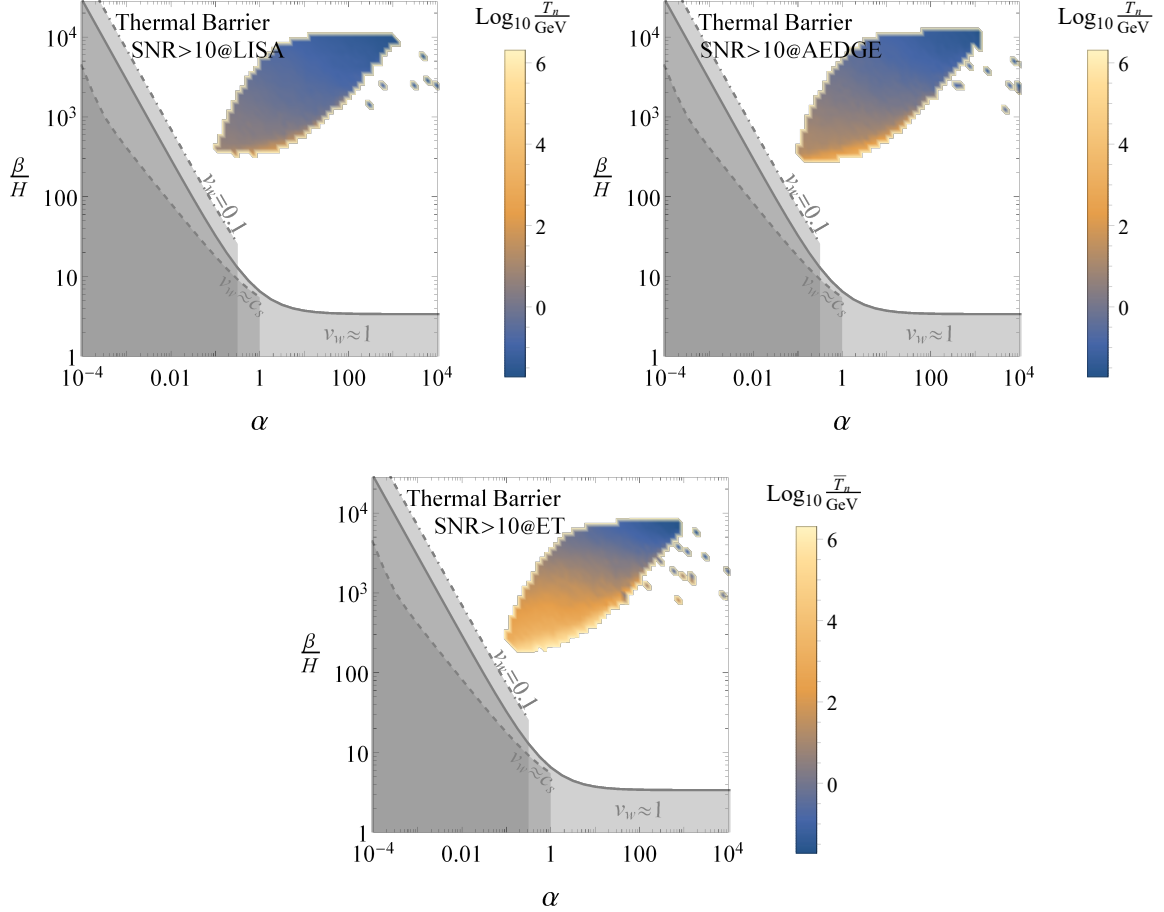


Figure 8: The coloured regions of the $(\alpha, \beta/H)$ planes feature a $\text{SNR} > 10$ for LISA (upper left panel), AEDGE (upper right panel) and ET (lower panel) for a potential with a pure thermal barrier. The color gradient corresponds to different values of the (average) phase transition nucleation temperature T_n in each case. The grey shading shows the regions with long-lived GW emission from sound waves ($H\tau_{\text{sh}} > 1$) for different bubble wall velocities.

As already mentioned, whilst the capabilities of LISA, ET and AEDGE to detect a GW signal from a first-order cosmological phase transition appear similar for α and β/H , they are sensitive to very different transition temperatures. To illustrate this explicitly, we show in Fig. 8 the average nucleation temperature T_n probed by the LISA (upper left panel), AEDGE (upper right panel) and ET (bottom panel) GW experiments, for the scenario with a purely thermal barrier discussed in Sec. 4.1, as a function of α and β/H , clearly showing the expected correlation, with experiments sensitive to lower frequency ranges being more sensitive to lower transition temperatures.

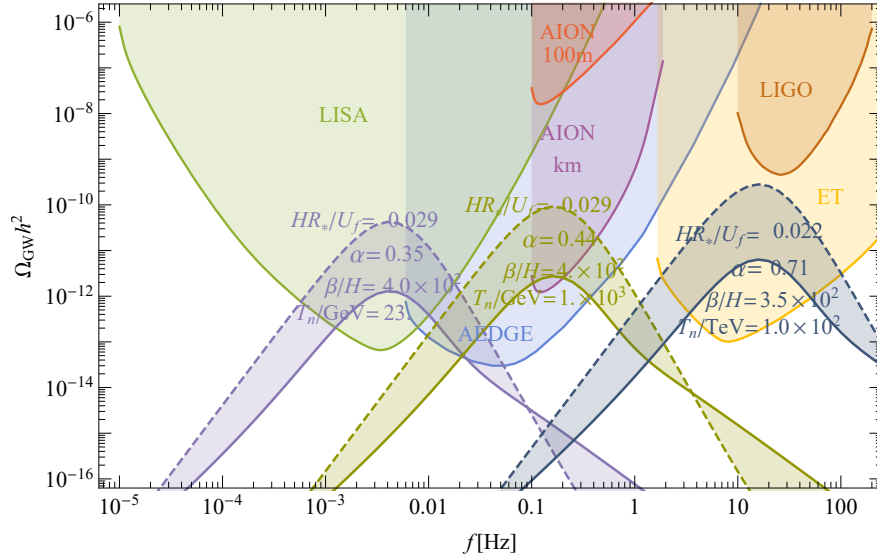


Figure 9: GW spectra for parameter choices with some of the highest SNR for LISA [13, 52], the Einstein Telescope (ET) [9, 53] and AEDGE [12] found in our scan of the scenario with a purely thermal potential barrier from Sec. 4.1. Solid lines show GW spectra as calculated in this work, while dashed lines show GW spectra calculated using older estimates from [5], which assumed that the sound wave period lasts for a Hubble time, i.e., $H\tau_{\text{sh}} > 1$. We also show the sensitivities of LIGO [8, 54, 55] and the terrestrial atom interferometer AION [11] (which is similar to that of MAGIS [10, 56]).

Finally, we also show for illustration in Figs. 9, 10 and 11 several GW spectra (solid lines) that would yield a high SNR in the LISA, AEDGE and ET experiments (we also depict the sensitivities of LIGO [8, 54, 55] and the proposed terrestrial atom interferometer AION [11], which has a similar sensitivity to that of the MAGIS [10, 56] experiment) in each of the models we have studied respectively in Sections 4.1, 4.2, and 4.3. In each case, we show for comparison (dashed lines) the GW spectra that would be calculated assuming that the sound waves could act as a GW source during an entire Hubble time. We see that in all cases the possible GW signals are reduced by one to two orders of magnitude when a more realistic estimate of the duration of the sound wave GW source is used. Even with these reductions in GW production due to the curtailment of the period of sound waves as an active GW source, we see that each of the three scenarios may produce detectable signals in any of LISA, AEDGE and ET. We note also that for some model parameters there are significant opportunities for measurements in a pair of detectors, illustrated by the facts that the optimal parameter choices for LISA would also yield observable signals in AEDGE, and vice versa, opening up the possibility of measuring the GW spectrum over a wide range of frequencies (see, e.g., [14] for a discussion). However, we note that the reductions in the GW strength diminish significantly the possibilities for MAGIS/AION and particularly for LIGO to detect GWs from a phase transition in the early Universe.

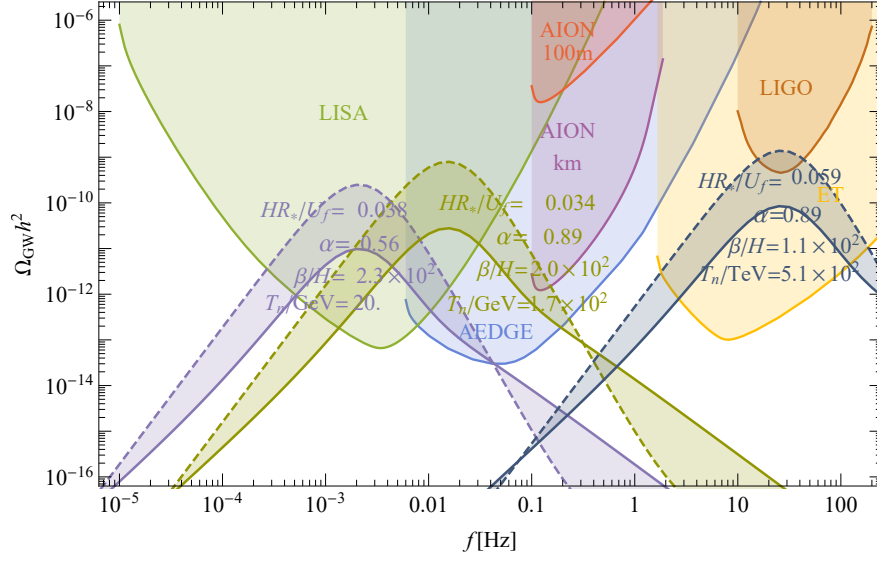


Figure 10: Same as Fig. 9, for the scenario with a zero-temperature barrier from Section 4.2.

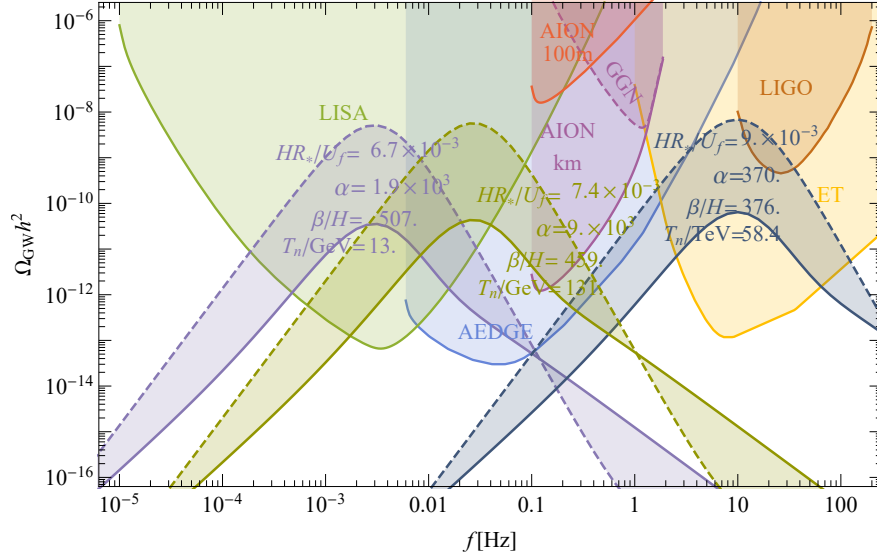


Figure 11: Same as Fig. 9, for the scenario with a scale-invariant Coleman-Weinberg-like potential from Section 4.3.

6 Conclusions

We have analyzed in this work the possible duration of a sound wave GW signal from a cosmological first-order phase transition, using simple polynomial forms of effective potential without and with a potential barrier at zero temperature, as well as a scale-invariant Coleman-Weinberg-like model. We have taken into account the various possible hydrodynamical solutions for the expansion of bubbles during the transition, namely deflagrations, detonations and hybrid solutions, depending on the value of the bubble expansion velocity

v_w , obtaining in each case the energy available for GW production in terms of v_w and the strength of the transition α . We have considered the emission of GWs by bubble collisions as well as by sound waves and by turbulence in the plasma following the transition, assuming for the latter that all the energy in the bulk fluid motion when the flow becomes nonlinear is available to create turbulence. Scanning over the parameter space of the different scenarios, we then identified the regions of the $(\alpha, \beta/H)$ plane (where β is the time scale for the transition) in which the future GW experiments LISA, the Einstein Telescope (ET) and AEDGE could detect GWs with a large signal-to-noise ratio, $\text{SNR} > 10$. The complementarity among the approved GW LISA experiment, the planned ET experiment and the proposed AEDGE atom interferometer space experiment is manifest in our Figs. 9, 10 and 11. LISA has optimal sensitivity at frequencies $\lesssim 10^{-2}$ Hz, whereas ET and AEDGE would have optimal sensitivities at frequencies ~ 10 Hz and frequencies $\sim 10^{-1}$ Hz, respectively. A combination of them might be needed to map out the full GW spectrum in any given model, as highlighted in our Figs. 9, 10 and 11. As seen in these Figures, the proposed 1-km versions of the terrestrial atom interferometers MAGIS and/or AION could also have some sensitivity to the models discussed in this paper.

When the first-order phase transition is of purely thermal origin (i.e., there is no zero-temperature barrier in the scalar potential), the regions of parameter space with $\text{SNR} > 10$ in the different experiments all correspond to a duration of the GW production from sound waves that is significantly less than a Hubble time. This is also true for most of the $(\alpha, \beta/H)$ parameter space of models with a zero-temperature potential barrier, although in this case there are small regions of parameter space where the duration may extend up to a Hubble time. All of the points in this region also correspond to substantial phase transition supercooling. The GW spectra calculated in this work are generally of smaller amplitude than those calculated using results from [5], which assumed that the sound-wave period lasts a Hubble time, i.e., $H\tau_{\text{sh}} = 1$. On the other hand, our GW spectra have broader extensions to higher frequencies, sourced by turbulence.

We stress that we have endeavoured to make our analysis as general as possible, extending the analysis of [7, 22] in the context of particular particle physics models. We have thus covered generic models whose effective potentials can be approximated by a polynomial as well as classically conformal, Coleman-Weinberg-like models. Although all these models generally predict short bursts of GWs from sound waves lasting much less than a Hubble time, we recognise the phenomenological interest of other forms of potential to which our analysis does not apply directly. Other shortcomings of our analysis include our assumption that all the energy in the bulk fluid motion when the flow becomes nonlinear is available to create turbulence that can source GWs, and uncertainties in the modelling of GW production from turbulence. Since the GW production during the nonlinear evolution of the plasma at the end of the phase transition is not yet known, our assumptions may not hold in general. These caveats aside, our analysis provides some encouragement that, despite the shortened sound wave period we find, future GW experiments may be able to probe the dynamics of a phase transition in the early universe over a wide range of frequencies, giving us direct access to the very early stages of the evolution of the Universe.

Acknowledgments

The work of JE and ML was supported by the UK STFC Grant ST/P000258/1. JE was also supported by the Estonian Research Council via a Mobilitas Pluss grant and ML by Polish

National Science Center grant 2018/31/D/ST2/02048. J.M.N. was supported by Ramón y Cajal Fellowship contract RYC-2017-22986, and also acknowledges support from the Spanish MINECO’s “Centro de Excelencia Severo Ochoa” Programme under grant SEV-2016-0597, from the European Union’s Horizon 2020 research and innovation programme under the Marie Skłodowska-Curie grant agreements 690575 (RISE InvisiblesPlus) and 674896 (ITN ELUSIVES) and from the Spanish Proyectos de I+D de Generación de Conocimiento via grant PGC2018-096646-A-I00.

A Further aspects of hydrodynamics

We identified in the main text three possibilities for the hydrodynamics of the transition, depending upon the bubble wall velocity v_w , which we consider here in turn.

- For wall velocities slower than the speed of sound of the plasma ($v_w < c_s$) we obtain a *deflagration*, in which the wall simply pushes the plasma shell around it;
- For larger wall velocities $v_w > c_s$, if the strength of the transition is sufficiently weak we have a *detonation* solution, in which the plasma shell follows the expanding wall;
- Finally for $v_w > c_s$ and a strong interaction with the plasma, we find a *hybrid* solution that, as the name suggests, combines the two behaviours mentioned above.

A.1 Detonations

We consider first the simplest case of the detonation solution. In this case the plasma shell follows the bubble wall, so that in the wall frame the plasma outside simply goes into the wall with speed $v_+ = v_w$. We can then find the velocity inside using Eq. (2.14), which yields

$$v_- = \frac{1 - 3\alpha + 3v_w^2(1 + \alpha) + \sqrt{(1 - 3\alpha + 3v_w^2(1 + \alpha))^2 - 12v_w^2}}{6v_w}, \quad (\text{A.1})$$

where we have set $\alpha_+ = \alpha$ (see Eq. (2.8)), as in this solution the bubble does not perturb the plasma outside and the value in our matching condition is the same as the global strength of the transition in the symmetric phase. For the above equation to have a positive solution we need

$$\alpha < \alpha_{\text{max}}^{\text{det}} = \frac{(1 - \sqrt{3}v_w)^2}{3(1 - v_w)}. \quad (\text{A.2})$$

If this is not fulfilled, a detonation solution is not realised, and we find instead a hybrid solution, which we discuss in detail in the last Section of this Appendix.

We are now ready to find the velocity and enthalpy profiles in the frame of the bubble. We simply need to solve Eqs. (2.14) and (2.15) inside the bubble, starting from the plasma velocity at the wall transformed into the bubble frame, and using the enthalpy given by the matching conditions:

$$v(\xi < v_w) = \frac{v_w - v_-}{1 - v_w v_-}, \quad \omega(\xi < v_w) = \frac{v_w}{1 - v_w^2} \frac{1 - v_-^2}{v_-}. \quad (\text{A.3})$$

The velocity goes smoothly to zero at $\xi = v_-$, and from that point remains constant just as ω as we approach the centre of the bubble ($\xi \rightarrow 0$). We show examples of resulting profiles in Fig. 12.

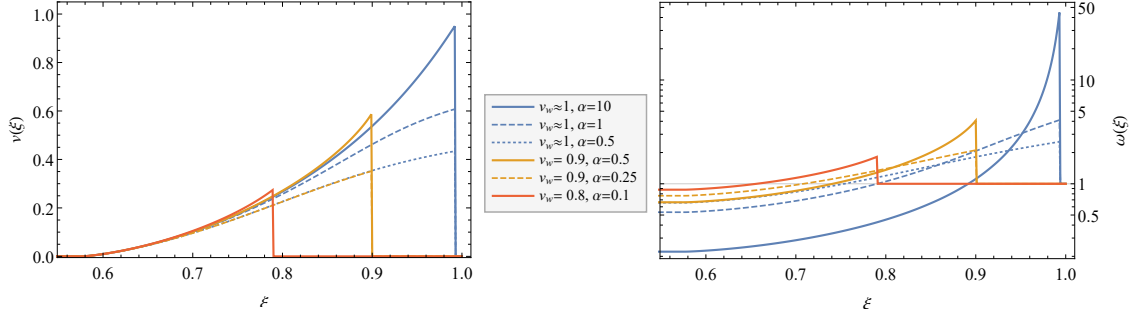


Figure 12: Left panel: Detonation plasma velocity profiles for three wall velocities and several possible strengths of the transition. Right panel: Enthalpy profile examples, normalised to the enthalpy in the symmetric background phase.

A.2 Deflagrations

The criterion for the realisation of a deflagration solution is simply that the wall velocity be subsonic: $\xi_w < c_s$. The plasma is at rest inside the wall in the frame of the bubble centre, which means that in the wall frame $v_- = \xi_w$, while the velocity outside is found using Eq. (2.14). The immediate issue here is that $\alpha_+ \neq \alpha$, as the latter is defined in the symmetric phase background and not in the heated plasma shell. Thus, we start with some value for α_+ and find α as an output of our calculation. We can then find the profile for a given α by scanning numerically over our input α_+ to find the desired strength of the transition.

Next we need to solve Eqs. (2.14) outside the wall, starting with

$$v(\xi > v_w) = \frac{v_w - v_+}{1 - v_w v_+}. \quad (\text{A.4})$$

The extra difficulty is that the only consistent solution ends with a shock front rather than the velocity decreasing smoothly. The shock front appears at ξ_{sh} defined by the condition

$$0 = \frac{c_s^2 - \xi^2}{(c_s^2 - 1)\xi} - v(\xi) \Big|_{\xi=\xi_{\text{sh}}}. \quad (\text{A.5})$$

The jump in velocity means that we must use again the matching conditions (2.11), this time for inside and outside the shock front. This also leads to an extra jump in the enthalpy profile, which we again solve inside the shock front using Eq. (2.15), and starting from

$$\omega(\xi_{\text{sh}}) = \frac{\xi_{\text{sh}}}{1 - \xi_{\text{sh}}^2} \frac{1 - v_{\text{sym}}^2}{v_{\text{sym}}}, \quad v_{\text{sym}} = \frac{\xi_{\text{sh}} - v(\xi_{\text{sh}})}{1 - \xi_{\text{sh}} v(\xi_{\text{sh}})}, \quad (\text{A.6})$$

where the second equality gives the velocity outside the shock front in the symmetric phase background. We can now use this result to match to the outside of the plasma shell and derive the strength of the transition to which our inputs correspond:

$$\alpha = \alpha_+ \omega(\xi = v_w). \quad (\text{A.7})$$

To calculate the enthalpy inside the bubble we need to include also the step at the bubble wall:

$$\omega(\xi < v_w) = \omega(\xi > v_w) \frac{1 - v_w^2}{v_w} \frac{v_+}{1 - v_+^2}, \quad (\text{A.8})$$

after which the enthalpy remains constant all the way to the centre of the bubble. We show examples of results from this calculation in the forms of velocity and enthalpy profiles in Fig. 13.

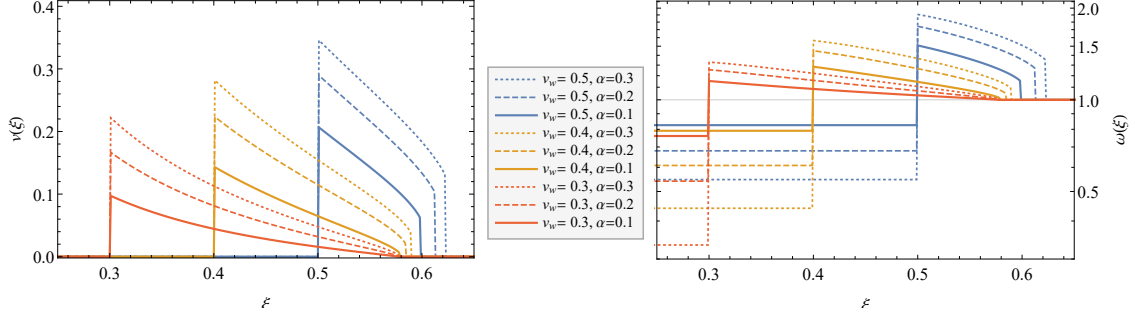


Figure 13: *Left panel: Deflagration plasma velocity profiles for three wall velocities and several possible strengths of the transition. Right panel: Enthalpy profile examples, normalised to the enthalpy in the symmetric background phase.*

A.3 Hybrids

We describe finally hybrid solutions that combine the features discussed in the previous subsections. These solutions are realised for supersonic wall velocities $v_w > c_s$ if the transition is so strong that the bound (A.2) is violated. This would mean we are dealing with a supersonic deflagration, as was shown in hydrodynamic simulations to be unstable and indeed to develop a rarefaction wave identical to a detonation [57].

As before, we start with the velocity profile computed using (2.14). Matching the velocities on both sides with detonation and deflagration constraints we see the wall velocity cannot be identified with the plasma velocity on either side. The only consistent choice is to set $v_- = c_s$ with v_+ given by (2.12). Just as in the deflagration case, $\alpha_{out} \neq \alpha$ due to the appearance of a shock front. Thus we again have to use α_{out} as our input and proceed to calculate the corresponding α .

To find the velocity inside the wall we start at the wall with

$$v(\xi < v_w) = \frac{v_w - v_-}{1 - v_w v_-}, \quad v(\xi > v_w) = \frac{v_w - v_+}{1 - v_w v_+}. \quad (\text{A.9})$$

We solve eq. (2.14) for $\xi = c_s$ inside the wall where the velocity reaches zero, and outside the bubble we solve until reaching the shock front, again defined by Eq. (A.5), at which the velocity drops to zero.

To find the enthalpy profile normalised to the symmetric phase outside the shock front, we use Eq. (A.6) just as in the deflagration case. We then again solve Eq. (2.15) until the bubble wall, where we introduce the necessary step

$$\omega(\xi < v_w) = \frac{1 - v_-^2}{v_-} \frac{v_+}{1 - v_+^2} \omega(\xi > v_w), \quad (\text{A.10})$$

and then continue to $\xi = c_s$, beyond which enthalpy does not change any more going towards the centre of the bubble.

As in the deflagration case, we find the strength of the transition corresponding to our input $\alpha = \alpha_+ \omega(\xi > v_w)$. We then find numerically the inputs matching the desired strength

of the transition. Examples of the resulting velocity and enthalpy profiles are shown in Fig. 14.

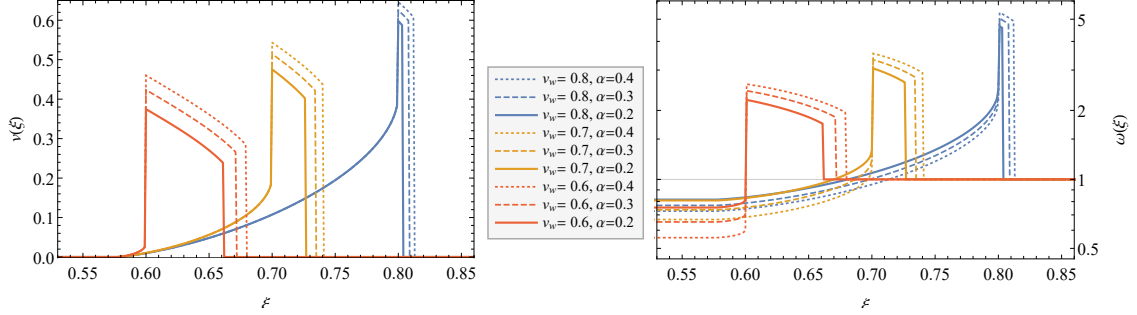


Figure 14: Left panel: Hybrid plasma velocity profiles for three wall velocities and several possible strengths of the transition. Right panel: Enthalpy profile examples, normalised to the enthalpy in the symmetric background phase.

B Percolation and successful completion of the transition

In specific models we encounter possible transitions with significant supercooling. In these cases the simple exponential nucleation approximation $\Gamma \propto e^{-\beta t}$ can fail (see eq. (2.6)), which is typically signalled by low values of β/H . In order to avoid this problem in our analysis we use the more refined analysis of percolation described in detail in [22].

Assuming we know the decay rate Γ , the probability of a given point still being in the false vacuum reads [58, 59]

$$P(t) = e^{-I(t)}, \quad I(t) = \frac{4\pi}{3} \int_{t_c}^t dt' \Gamma(t') a(t')^3 r(t, t')^3, \quad (\text{B.1})$$

where a is the FRW scale factor and $r(t, t')$ is the radius of a bubble that nucleated at t' after growing until time t :

$$r(t, t') = \int_{t'}^t \frac{v_w d\tilde{t}}{a(\tilde{t})}. \quad (\text{B.2})$$

To solve for the scale factor we need the Friedmann equation including the radiation energy density ρ_R (we assume instantaneous reheating) and the energy density of the unstable vacuum ρ_V :

$$H(T)^2 = \frac{1}{3M_{\text{pl}}^2} (\rho_R + \rho_V) = \frac{1}{3M_{\text{pl}}^2} \left(\frac{T^4}{\xi_g^2} + \Delta V \right), \quad (\text{B.3})$$

with $\xi_g = \sqrt{30/(\pi^2 g_*)}$, where $g_* = 106.75$ is the number of degrees of freedom, and $M_{\text{pl}} = 2.435 \times 10^{18}$ GeV. Using Equation (B.1), the integrand of Equation (B.2) can be conveniently rewritten as function of temperature in terms of the product

$$a(T') r(T, T') = a(T') \int_T^{T'} \frac{v_w d\tilde{T}}{\tilde{T} H(\tilde{T}) a(\tilde{T})} = \frac{1}{T'} \int_T^{T'} \frac{v_w d\tilde{T}}{H(\tilde{T})}, \quad (\text{B.4})$$

which can readily be computed in terms of elliptic functions, yielding

$$I(T) = \frac{4\pi}{3} \int_T^{T_c} \frac{dT' \Gamma(T')}{T'^4 H(\tilde{T})} \left(\int_T^{T'} \frac{v_w d\tilde{T}}{H(\tilde{T})} \right)^3. \quad (\text{B.5})$$

We can now define the time of percolation as $P(T_*) = 1/e$, corresponding to $I(T_*) = 1$ [42]. Finally, the necessary requirement for successful completion of the transition concerns the physical volume of the false vacuum $\mathcal{V}_{\text{false}} \propto a(t)^3 P(t)$, which starts decreasing at the percolation [60]. This is a strong requirement, particularly in cases where vacuum energy dominates the expansion, since the probability $P(t)$ now has to decrease faster than the increase in the volume of the inflating space. This condition can be conveniently rewritten as

$$\frac{1}{\mathcal{V}_{\text{false}}} \frac{d\mathcal{V}_{\text{false}}}{dt} \Big|_{t=t_*} = 3H(t) - \frac{dI(t)}{dt} \Big|_{t=t_*} = H(T) \left(3 + T \frac{dI(T)}{dT} \right) \Big|_{T=T_*} < 0. \quad (\text{B.6})$$

In our analysis of concrete models in the remainder of this Section we always calculate the percolation temperature and check that the above constraint is fulfilled.

Let us also point out that in cases with a lot of supercooling the simple relation between the time scale and bubble size $H R_* = (8\pi)^{1/3} (\beta/H)^{-1}$ breaks down together with the definition of β (2.6). Then the more appropriate way to find the relevant scale for the transition is to compute the bubble size directly from the bubble number density [22]

$$n_B = (R_{*R})^{-3} = \int_{t_c}^t dt' \frac{a(t')^3}{a(t)^3} \Gamma(t') P(t'). \quad (\text{B.7})$$

Then we indeed find that points with very low β/H values always predict large but allowed bubble sizes $H R_* < 1$, contrary to what one would find naively assuming exponential nucleation.

C Analytic phase transition parameters

We quote here the explicit analytical formulae for parameters of the phase transitions in models discussed in Section 4.

C.1 Polynomial with only a thermal barrier

We start with the polynomial potential with purely thermal barrier we discussed in Section 4.1. The strength and duration of the transition read

$$\alpha = \frac{15 (\sqrt{9-4\delta} + 3) (-4\delta + 3\sqrt{9-4\delta} + 9) g_m^2 (48\pi^2 g_{m^2} \lambda - \delta g_m^2)}{32 \times 24^4 \pi^6 \sqrt{9-4\delta} g_* \lambda^3} \quad (\text{C.1})$$

and

$$\frac{\beta}{H} = \frac{2\sqrt{\delta} [-\beta_1(\delta+6) + \beta_2\delta(\delta-10) + \beta_3\delta^2(3\delta-14)] (48\pi^2 g_{m^2} \lambda - \delta g_m^2)}{243(\delta-2)^3 g_m \lambda^{3/2}}. \quad (\text{C.2})$$

These are both independent of temperature, other than through the dimensionless parameter δ . We can also easily calculate the nucleation temperature, which may be approximated by solving

$$\frac{\Gamma}{H^4} = \frac{T^4 e^{-\frac{S_3}{T}}}{\rho_R + \rho_V} = \frac{e^{-\frac{2g_m \left(\frac{\delta}{\lambda}\right)^{3/2} (\beta_1 + \beta_2 \delta + \beta_3 \delta^2)}}{243(\delta-2)^2}}{\left(\frac{T_0^2}{1 - \frac{g_m^2 \delta}{48\pi^2 g_{m^2} \lambda}} \right)^2 \left(\frac{1}{3M_p^2} \right)^2 \left(\frac{\pi^2 g_*}{30} + g_m^4 \frac{(\sqrt{9-4\delta}+3)^2 (\sqrt{9-4\delta}+3-2\delta)}{128 \times 24^4 \pi^4 \lambda^3} \right)^2} = 1, \quad (\text{C.3})$$

where we converted the temperature in the Hubble rate into δ using Eqs. (4.1), (4.2) and (4.3). This simplifies the calculation significantly, allowing us easily to solve numerically the equation, using the fact that varying the temperature in the interesting range from T_0 to T_c simply means varying δ from 0 to 2.

C.2 Zero-temperature barrier

We now proceed to the polynomial potential model with a barrier also present at $T = 0$, discussed in Section 4.2. The strength and duration of the transition read

$$\alpha = -\frac{5(\sqrt{9-4\delta}+3)g_{m^2}^2}{512\pi^2\sqrt{9-4\delta}g_*\lambda(3A^2\delta+\lambda T_0^2g_{m^2})^2}\left[3A^4\left\{2(\sqrt{9-4\delta}+6)\delta-9(\sqrt{9-4\delta}+3)\right\}+\right. \\ \left.+A^2\left\{4\delta-3(\sqrt{9-4\delta}+3)\right\}\lambda T_0^2g_{m^2}\right] \quad (\text{C.4})$$

and

$$\frac{\beta}{H} = \frac{8\pi\sqrt{\frac{\delta}{\lambda}}g_{m^2}\sqrt{\frac{3A^2\delta}{\lambda g_{m^2}}+T_0^2}}{243(\delta-2)^3(3A^3\delta+A\lambda T_0^2g_{m^2})}\left[-6A^2\delta\{\beta_1(\delta+2)+4\beta_2\delta-\beta_3\delta^2(\delta-6)\}+\right. \\ \left.-\lambda T_0^2g_{m^2}\{\beta_1(\delta+6)-\beta_2\delta(\delta-10)+\beta_3\delta^2(14-3\delta)\}\right]. \quad (\text{C.5})$$

We again express all temperature dependence through the dimensionless parameter δ . To calculate the nucleation temperature of the bubbles we need to solve

$$\frac{\Gamma}{H^4} = \frac{T^4 e^{-\frac{S_3}{T}}}{\rho_R + \rho_V} = \\ = \frac{\left(\frac{3A^2\delta}{\lambda g_{m^2}} + T_0^2\right)^2 e^{\frac{8\pi A\left(\frac{\delta}{\lambda}\right)^{3/2}(\beta_1+\delta(\beta_2+\beta_3\delta))}{81(\delta-2)^2\sqrt{\frac{3A^2\delta}{\lambda g_{m^2}}+T_0^2}}}}{\left(\frac{1}{3M_p^2}\right)^2 \left(\frac{\pi^2}{30}g_*\left(\frac{3A^2\delta}{\lambda g_{m^2}} + T_0^2\right)^2 + \frac{A^4\left(\sqrt{\frac{4\lambda T_0^2g_{m^2}}{3A^2}+9+3}\right)^2\left(\frac{2\lambda T_0^2g_{m^2}}{3A^2} + \sqrt{\frac{4\lambda T_0^2g_{m^2}}{3A^2}+9+3}\right)}{2048\lambda^3}\right)} = 1, \quad (\text{C.6})$$

where we converted the temperature in the Hubble rate into δ using Eqs. (4.1), (4.2) and (4.6). The calculation is slightly more complicated due to presence of a barrier at tree level. Essentially, one needs to find a minimum of Eq. (C.6) setting the minimal value of δ_{\min} , which might not exist if the barrier is too large and tunnelling too suppressed. If this is not the case and $\Gamma/H|_{\delta=\delta_{\min}} < 1$, we can find a solution varying δ from δ_{\min} to 2.

C.3 Classically scale-invariant potential

Finally, we proceed to the case of classically scale-invariant potential discussed in Section 4.3. We can express the key parameters of the transition as

$$\alpha = \frac{5(1-\delta)}{g_*\delta^2}, \\ \frac{\beta}{H} = \frac{\pi^3 I^3 2^{n_\mu+6} \delta^{n_\mu-\frac{1}{2}}}{9g^3v(2\delta-1)^3} \left[2\delta^4\mu_3 - \delta^3(2\mu_2+5\mu_3) - 3\delta^2(2\mu_1+\mu_2) + \right. \\ \left. -\delta(\mu_1+10) + 2(2\delta-1)(\delta^3\mu_3 + \delta^2\mu_2 + \delta\mu_1 + 1)n_\mu + 1\right]. \quad (\text{C.7})$$

We can also determine the nucleation temperature by solving

$$\frac{\Gamma}{H^4} = \frac{T^4 e^{-\frac{S_3}{T}}}{\rho_R + \rho_V} = \frac{\frac{9\delta^2 g^4 v^4}{4\pi^4} e^{-\frac{64\pi^3 I^3 (2\delta)^{n_\mu} (1+\mu_1\delta+\mu_2\delta^2+\mu_3\delta^3)}{9g^3 v \sqrt{\delta(1-2\delta)^2}}}}{\left(\frac{1}{3M_p^2}\right)^2 \left(\frac{\pi^2}{30} g_* \frac{9\delta^2 g^4 v^4}{4\pi^4} + \frac{3(1-2\delta)g^4 v^4}{8\pi^2}\right)^2} = 1, \quad (\text{C.8})$$

where we again converted the temperature into δ using Eq. (4.11). As in the previous cases, we have to solve the above numerically, varying from $\delta = 0$, which corresponds to zero temperature, to $\delta = 1/2$, which corresponds to the critical temperature.

References

- [1] A. G. Cohen, D. B. Kaplan and A. E. Nelson, *Progress in electroweak baryogenesis*, *Ann. Rev. Nucl. Part. Sci.* **43** (1993) 27–70, [[hep-ph/9302210](#)].
- [2] M. Trodden, *Electroweak baryogenesis*, *Rev. Mod. Phys.* **71** (1999) 1463–1500, [[hep-ph/9803479](#)].
- [3] D. E. Morrissey and M. J. Ramsey-Musolf, *Electroweak baryogenesis*, *New J. Phys.* **14** (2012) 125003, [[1206.2942](#)].
- [4] A. Beniwal, M. Lewicki, J. D. Wells, M. White and A. G. Williams, *Gravitational wave, collider and dark matter signals from a scalar singlet electroweak baryogenesis*, *JHEP* **08** (2017) 108, [[1702.06124](#)].
- [5] C. Caprini et al., *Science with the space-based interferometer eLISA. II: Gravitational waves from cosmological phase transitions*, *JCAP* **1604** (2016) 001, [[1512.06239](#)].
- [6] C. Caprini and D. G. Figueroa, *Cosmological Backgrounds of Gravitational Waves*, *Class. Quant. Grav.* **35** (2018) 163001, [[1801.04268](#)].
- [7] C. Caprini et al., *Detecting gravitational waves from cosmological phase transitions with LISA: an update*, *JCAP* **2003** (2020) 024, [[1910.13125](#)].
- [8] LIGO SCIENTIFIC collaboration, J. Aasi et al., *Advanced LIGO*, *Class. Quant. Grav.* **32** (2015) 074001, [[1411.4547](#)].
- [9] M. Punturo et al., *The Einstein Telescope: A third-generation gravitational wave observatory*, *Class. Quant. Grav.* **27** (2010) 194002.
- [10] MAGIS collaboration, P. W. Graham, J. M. Hogan, M. A. Kasevich, S. Rajendran and R. W. Romani, *Mid-band gravitational wave detection with precision atomic sensors*, [[1711.02225](#)].
- [11] L. Badurina et al., *AION: An Atom Interferometer Observatory and Network*, [[1911.11755](#)].
- [12] Y. A. El-Neaj et al., *AEDGE: Atomic Experiment for Dark Matter and Gravity Exploration in Space*, [[1908.00802](#)].
- [13] LISA collaboration, H. Audley et al., *Laser Interferometer Space Antenna*, [[1702.00786](#)].
- [14] D. G. Figueroa, E. Megias, G. Nardini, M. Pieroni, M. Quiros, A. Ricciardone et al., *LISA as a probe for particle physics: electroweak scale tests in synergy with ground-based experiments*, [[1806.06463](#)].
- [15] J. Ellis, M. Fairbairn, M. Lewicki, V. Vaskonen and A. Wickens, *Intergalactic Magnetic Fields from First-Order Phase Transitions*, *JCAP* **1909** (2019) 019, [[1907.04315](#)].
- [16] M. Hindmarsh, S. J. Huber, K. Rummukainen and D. J. Weir, *Gravitational waves from the sound of a first order phase transition*, *Phys. Rev. Lett.* **112** (2014) 041301, [[1304.2433](#)].

- [17] M. Hindmarsh, S. J. Huber, K. Rummukainen and D. J. Weir, *Numerical simulations of acoustically generated gravitational waves at a first order phase transition*, *Phys. Rev.* **D92** (2015) 123009, [[1504.03291](#)].
- [18] M. Hindmarsh, *Sound shell model for acoustic gravitational wave production at a first-order phase transition in the early Universe*, *Phys. Rev. Lett.* **120** (2018) 071301, [[1608.04735](#)].
- [19] M. Hindmarsh, S. J. Huber, K. Rummukainen and D. J. Weir, *Shape of the acoustic gravitational wave power spectrum from a first order phase transition*, *Phys. Rev.* **D96** (2017) 103520, [[1704.05871](#)].
- [20] M. Hindmarsh and M. Hijazi, *Gravitational waves from first order cosmological phase transitions in the Sound Shell Model*, *JCAP* **1912** (2019) 062, [[1909.10040](#)].
- [21] J. Ellis, M. Lewicki, J. M. No and V. Vaskonen, *Gravitational wave energy budget in strongly supercooled phase transitions*, *JCAP* **1906** (2019) 024, [[1903.09642](#)].
- [22] J. Ellis, M. Lewicki and J. M. No, *On the Maximal Strength of a First-Order Electroweak Phase Transition and its Gravitational Wave Signal*, *JCAP* **1904** (2019) 003, [[1809.08242](#)].
- [23] A. D. Linde, *Fate of the False Vacuum at Finite Temperature: Theory and Applications*, *Phys. Lett.* **B100** (1981) 37.
- [24] A. D. Linde, *Decay of the False Vacuum at Finite Temperature*, *Nucl. Phys.* **B216** (1983) 421.
- [25] A. Megevand and S. Ramirez, *Bubble nucleation and growth in very strong cosmological phase transitions*, *Nucl. Phys.* **B919** (2017) 74–109, [[1611.05853](#)].
- [26] R. Jinno, S. Lee, H. Seong and M. Takimoto, *Gravitational waves from first-order phase transitions: Towards model separation by bubble nucleation rate*, *JCAP* **1711** (2017) 050, [[1708.01253](#)].
- [27] D. Cutting, M. Hindmarsh and D. J. Weir, *Gravitational waves from vacuum first-order phase transitions: from the envelope to the lattice*, *Phys. Rev.* **D97** (2018) 123513, [[1802.05712](#)].
- [28] S. Coleman, *Aspects of Symmetry*. Cambridge University Press, Cambridge, U.K., 1985, [10.1017/CBO9780511565045](#).
- [29] P. J. Steinhardt, *Relativistic Detonation Waves and Bubble Growth in False Vacuum Decay*, *Phys. Rev.* **D25** (1982) 2074.
- [30] J. Ignatius, K. Kajantie, H. Kurki-Suonio and M. Laine, *The growth of bubbles in cosmological phase transitions*, *Phys. Rev.* **D49** (1994) 3854–3868, [[astro-ph/9309059](#)].
- [31] J. R. Espinosa, T. Konstandin, J. M. No and G. Servant, *Energy Budget of Cosmological First-order Phase Transitions*, *JCAP* **1006** (2010) 028, [[1004.4187](#)].
- [32] S. Yu. Khlebnikov, *Fluctuation - dissipation formula for bubble wall velocity*, *Phys. Rev.* **D46** (1992) R3223–R3226.
- [33] P. B. Arnold, *One loop fluctuation - dissipation formula for bubble wall velocity*, *Phys. Rev.* **D48** (1993) 1539–1545, [[hep-ph/9302258](#)].
- [34] G. D. Moore and T. Prokopec, *Bubble wall velocity in a first order electroweak phase transition*, *Phys. Rev. Lett.* **75** (1995) 777–780, [[hep-ph/9503296](#)].
- [35] G. D. Moore and T. Prokopec, *How fast can the wall move? A Study of the electroweak phase transition dynamics*, *Phys. Rev.* **D52** (1995) 7182–7204, [[hep-ph/9506475](#)].
- [36] P. John and M. G. Schmidt, *Do stops slow down electroweak bubble walls?*, *Nucl. Phys.* **B598** (2001) 291–305, [[hep-ph/0002050](#)].
- [37] A. Megevand and A. D. Sanchez, *Velocity of electroweak bubble walls*, *Nucl. Phys.* **B825** (2010) 151–176, [[0908.3663](#)].

- [38] S. J. Huber and M. Sopena, *The bubble wall velocity in the minimal supersymmetric light stop scenario*, *Phys. Rev.* **D85** (2012) 103507, [[1112.1888](#)].
- [39] J. Kozaczuk, *Bubble Expansion and the Viability of Singlet-Driven Electroweak Baryogenesis*, *JHEP* **10** (2015) 135, [[1506.04741](#)].
- [40] G. C. Dorsch, S. J. Huber and T. Konstandin, *Bubble wall velocities in the Standard Model and beyond*, *JCAP* **1812** (2018) 034, [[1809.04907](#)].
- [41] U.-L. Pen and N. Turok, *Shocks in the Early Universe*, *Phys. Rev. Lett.* **117** (2016) 131301, [[1510.02985](#)].
- [42] K. Enqvist, J. Ignatius, K. Kajantie and K. Rummukainen, *Nucleation and bubble growth in a first order cosmological electroweak phase transition*, *Phys. Rev.* **D45** (1992) 3415–3428.
- [43] S. R. Coleman, *The Fate of the False Vacuum. 1. Semiclassical Theory*, *Phys. Rev.* **D15** (1977) 2929–2936.
- [44] L. Darmé, J. Jaeckel and M. Lewicki, *Towards the fate of the oscillating false vacuum*, *Phys. Rev.* **D96** (2017) 056001, [[1704.06445](#)].
- [45] F. C. Adams, *General solutions for tunneling of scalar fields with quartic potentials*, *Phys. Rev.* **D48** (1993) 2800–2805, [[hep-ph/9302321](#)].
- [46] M. Quiros, *Finite temperature field theory and phase transitions*, in *Proceedings, Summer School in High-energy physics and cosmology: Trieste, Italy, June 29-July 17, 1998*, pp. 187–259, 1999, [[hep-ph/9901312](#)], <http://alice.cern.ch/format/showfull?sysnb=0302087>.
- [47] D. Bodeker and G. D. Moore, *Electroweak Bubble Wall Speed Limit*, *JCAP* **1705** (2017) 025, [[1703.08215](#)].
- [48] D. Bodeker and G. D. Moore, *Can electroweak bubble walls run away?*, *JCAP* **0905** (2009) 009, [[0903.4099](#)].
- [49] M. Kamionkowski, A. Kosowsky and M. S. Turner, *Gravitational radiation from first order phase transitions*, *Phys. Rev.* **D49** (1994) 2837–2851, [[astro-ph/9310044](#)].
- [50] C. Caprini, R. Durrer and G. Servant, *The stochastic gravitational wave background from turbulence and magnetic fields generated by a first-order phase transition*, *JCAP* **0912** (2009) 024, [[0909.0622](#)].
- [51] D. Cutting, M. Hindmarsh and D. J. Weir, *Vorticity, kinetic energy, and suppressed gravitational wave production in strong first order phase transitions*, [[1906.00480](#)].
- [52] N. Bartolo et al., *Science with the space-based interferometer LISA. IV: Probing inflation with gravitational waves*, *JCAP* **1612** (2016) 026, [[1610.06481](#)].
- [53] S. Hild et al., *Sensitivity Studies for Third-Generation Gravitational Wave Observatories*, *Class. Quant. Grav.* **28** (2011) 094013, [[1012.0908](#)].
- [54] E. Thrane and J. D. Romano, *Sensitivity curves for searches for gravitational-wave backgrounds*, *Phys. Rev.* **D88** (2013) 124032, [[1310.5300](#)].
- [55] VIRGO, LIGO SCIENTIFIC collaboration, B. P. Abbott et al., *GW150914: Implications for the stochastic gravitational wave background from binary black holes*, *Phys. Rev. Lett.* **116** (2016) 131102, [[1602.03847](#)].
- [56] P. W. Graham, J. M. Hogan, M. A. Kasevich and S. Rajendran, *Resonant mode for gravitational wave detectors based on atom interferometry*, *Phys. Rev.* **D94** (2016) 104022, [[1606.01860](#)].
- [57] H. Kurki-Suonio and M. Laine, *Supersonic deflagrations in cosmological phase transitions*, *Phys. Rev.* **D51** (1995) 5431–5437, [[hep-ph/9501216](#)].

- [58] A. H. Guth and S. H. H. Tye, *Phase Transitions and Magnetic Monopole Production in the Very Early Universe*, *Phys. Rev. Lett.* **44** (1980) 631.
- [59] A. H. Guth and E. J. Weinberg, *Cosmological Consequences of a First Order Phase Transition in the $SU(5)$ Grand Unified Model*, *Phys. Rev.* **D23** (1981) 876.
- [60] M. S. Turner, E. J. Weinberg and L. M. Widrow, *Bubble nucleation in first order inflation and other cosmological phase transitions*, *Phys. Rev.* **D46** (1992) 2384–2403.